remote sensing

MDPI

Article

An Ensemble Learning Approach for Landslide Susceptibility Assessment Considering Spatial Heterogeneity Partitioning and Feature Selection

Xiangchao Jiang [1], Zhen Yang [1,2,3,*], Hongbo Mei [4], Meinan Zheng [1,2,3], Jiajia Yuan [1,5] and Lei Wang [1,2,3]

[1] School of Geomatics, Anhui University of Science and Technology, Huainan 232001, China; xcjiang@aust.edu.cn (X.J.); zhengmn@aust.edu.cn (M.Z.); jiajia.yuan@polyu.edu.hk (J.Y.); lwang@aust.edu.cn (L.W.)
[2] Coal Industry Engineering Research Center of Mining Area Environmental and Disaster Cooperative Monitoring, Anhui University of Science and Technology, Huainan 232001, China
[3] Key Laboratory of Aviation-Aerospace-Ground Cooperative Monitoring and Early Warning of Coal Mining-Induced Disasters of Anhui Higher Education Institutes, Anhui University of Science and Technology, Huainan 232001, China
[4] School of Earth Resources, China University of Geosciences, Wuhan 430074, China; hbmei@cug.edu.cn
[5] Department of Land Surveying and Geo-Informatics, The Hong Kong Polytechnic University, Hong Kong 999077, China
* Correspondence: yangzhen@aust.edu.cn

Abstract

Traditional landslide susceptibility assessment (LSA) methods typically adopt a global modeling strategy, which struggles to account for the pronounced spatial heterogeneity arising from variations in topography, geology, and vegetation conditions within a region. Furthermore, model predictive performance is often undermined by feature redundancy. To address these limitations, this study focuses on the landslide disaster early-warning demonstration area in Honghe Prefecture, Yunnan Province. It proposes an ensemble learning model termed heterogeneity feature optimized stacking (HF-stacking), which integrates spatial heterogeneity partitioning (SHP) with feature selection to improve the scientific rigor of LSA. This method initially establishes an LSA system comprising 15 static landslide conditioning factors (LCFs) and two dynamic factors representing the average annual deformation rates derived from interferometric synthetic aperture radar (InSAR) technology. Based on landslide inventory data, an SHP method combining t-distributed stochastic neighbor embedding (t-SNE) and iterative self-organizing (ISO) clustering was developed to divide the study area into subregions. Within each subregion, a tailored feature selection strategy was applied to determine the optimal feature subset. The final LSA was performed using the stacking ensemble learning approach. The results show that the HF-stacking model achieved the best overall performance, with an average AUC of 95.90% across subregions, 4.23% higher than the traditional stacking model. Other evaluation metrics also demonstrated comprehensive improvements. This study confirms that constructing an SHP framework and implementing feature selection strategies can effectively reduce the impact of spatial heterogeneity and feature redundancy, thereby significantly enhancing the predictive performance of LSA models. The proposed method contributes to improving the reliability of regional landslide risk assessments.

Keywords: spatial heterogeneity; stacking ensemble learning; feature selection; deep learning; landslide susceptibility assessment

check for updates

Academic Editor: Michele Saroli

Received: 20 June 2025
Revised: 22 July 2025
Accepted: 6 August 2025
Published: 18 August 2025

Citation: Jiang, X.; Yang, Z.; Mei, H.; Zheng, M.; Yuan, J.; Wang, L. An Ensemble Learning Approach for Landslide Susceptibility Assessment Considering Spatial Heterogeneity Partitioning and Feature Selection. *Remote Sens.* **2025**, *17*, 2875. https://doi.org/10.3390/rs17162875

1. Introduction

As one of the most common and dangerous geological events, landslides pose a significant global threat. They are characterized by suddenness and high frequency due to various environmental factors, endangering human lives and causing substantial damage to assets and infrastructure [1]. To reduce these risks, landslide susceptibility assessment (LSA) has become a vital tool for identifying areas at risk of landslides and supporting early-warning systems and risk management strategies. By analyzing landslide conditioning factors (LCFs), LSA predicts the likelihood of landslide occurrences and provides critical scientific data to help in disaster prevention and mitigation efforts [2].

In recent decades, LSA methods have experienced significant development, covering a wide range of approaches—from knowledge-based strategies to advanced machine learning models. Traditional LSA methods are usually divided into knowledge-based approaches and statistical analysis models [3]. Among these, techniques such as the information value (IV), certainty factor (CF), and frequency ratio (FR) models are commonly employed due to their simplicity and interpretability [4–6]. However, these statistical models often rely on assumptions of linearity or conditional independence among variables, which restricts their ability to identify complex nonlinear relationships and high-order interactions between LCFs and landslide events. Additionally, these methods are highly sensitive to data quality; imbalanced sample distributions or spatial biases can lead to inaccurate or distorted susceptibility assessments [7,8]. With ongoing research advancements and rapid developments in artificial intelligence, recent progress in LSA methodologies can be categorized into three groups: machine learning (ML), deep learning (DL), and ensemble learning (EL) models. ML has been widely adopted in LSA owing to its capacity to model nonlinear associations between landslides and LCFs. Commonly used ML models include random forest (RF), support vector machine (SVM), and extreme gradient boosting (XGBoost) [9,10]. Additionally, DL, a subset of machine learning, has rapidly advanced both theoretically and practically. DL models such as convolutional neural networks (CNN) [11,12], multi-layer perceptron (MLP) [13], and deep neural networks (DNN) [14] utilize multi-layer structures to identify nonlinear relationships and effectively capture deeper, intrinsic characteristics among factors. Consequently, these models have been increasingly integrated into LSA research and applications [15–18]. EL aims to improve the predictive performance of models by combining the strengths of multiple learners. Currently, traditional ensemble frameworks, including bagging, boosting, stacking, and blending, have been applied to integrate traditional ML and DL models for LSA [19–22]. These models have demonstrated superior prediction accuracy compared to individual models [23]. Additionally, research indicates that EL enhances robustness to unseen data by combining the complementary strengths of various models, resulting in more reliable predictive outcomes [24,25].

In LSA research, spatial heterogeneity describes differences in LCFs across geographic areas, especially in mountainous regions with diverse terrain and complex geology. This variability directly impacts the likelihood and magnitude of landslide events [26]. Recent advances have been made in addressing spatial heterogeneity within LSA studies. For example, Chang et al. [27] introduced a climate-based regionalization strategy, whereby the study area was partitioned according to climatic characteristics to improve the adaptability of the model to distinct spatial units. Liu and Chen [28] employed the agglomerative nesting (AGNES) clustering algorithm to partition global raster units into multiple local sub-regions. Their findings indicate that methods accounting for spatial heterogeneity achieve superior accuracy and robustness compared to traditional approaches. Building upon the above studies, this research addresses the common issue in clustering analysis wherein the distance between samples becomes increasingly uniform in high-dimensional environmental feature space, thereby diminishing the discriminative power of clustering [29], this research presents an innovative approach that combines the nonlinear embedding technique t-distributed stochastic neighbor embedding (t-SNE) with the clustering algorithm iterative self-organizing (ISO) for spatial heterogeneity partitioning (SHP). First, the t-SNE algorithm is applied to compress the high-dimensional LCFs data. This method possesses strong nonlinear embedding capabilities, effectively preserving the local structural features of the data and thereby enhancing the separability of subsequent clustering and the interpretability of spatial partitioning [30]. Subsequently, ISO clustering analysis is conducted to enhance data effectiveness. Additionally, information redundancy among LCFs can significantly decrease the predictive accuracy of LSA models [31,32]. Significant progress has been achieved, and current mainstream feature selection methods can be categorized into collinearity analysis and importance analysis. The former mainly employs statistical techniques such as Pearson correlation coefficients and variance inflation factors for preliminary feature selection [33,34]. However, these methods are insufficient in capturing the underlying associations between features and landslide events. Conversely, importance analysis employs techniques such as GeoDetector [35] and model interpretation methods, including SHAP values, to quantitatively assess how each factor contributes to the observed pattern of landslide distribution [36–38]. To address the limitations of traditional unidimensional feature selection methods, this study further innovates by introducing a hybrid strategy that integrates collinearity and importance analyses.

In this research, the landslide disaster warning demonstration area of Honghe Hani and Yi Autonomous Prefecture in Yunnan Province was selected as our research area. interferometric synthetic aperture radar (InSAR) technology was employed to acquire dynamic LCFs, which were combined with static factors to develop a comprehensive LSA system. Subsequently, the t-SNE-ISO algorithm was applied to delineate subregions within the study area, effectively minimizing the impact of spatial heterogeneity. Additionally, a feature selection strategy was implemented to choose the most effective set of factors, leading to the creation of a landslide susceptibility map (LSM) using the stacking ensemble algorithm.

2. Study Area and Materials

2.1. Study Area

The landslide disaster warning demonstration area, as depicted in Figure 1, lies within the Honghe Hani and Yi Autonomous Prefecture, encompassing the counties of Jinping, Pingbian, and Hekou in Yunnan Province, China. The region is situated between longitudes 102°31′33″–104°16′42″E and latitudes 22°26′40″–23°23′25″N, covering approximately 6915 km^2. Situated near the Tropic of Cancer, the region experiences a low-latitude, subtropical humid monsoon climate characteristic of mountainous areas. It receives approximately 2000.9 mm of annual rainfall and maintains an average temperature of 19.1 °C throughout the year. The rainy season spans from June to August, during which geological disasters frequently occur. The area is predominantly mountainous, with elevations ranging from 76 to 3074 m, and approximately 70.49% of the region is higher than 800 m. The hydrological network is highly developed, with dense river systems that increase erosion, resulting in steep slopes and active gravitational geological processes. In recent years, intensified human engineering activities have required extensive slope removal for infrastructure projects. These factors provide the physical conditions that promote the initiation of landslide geological processes.

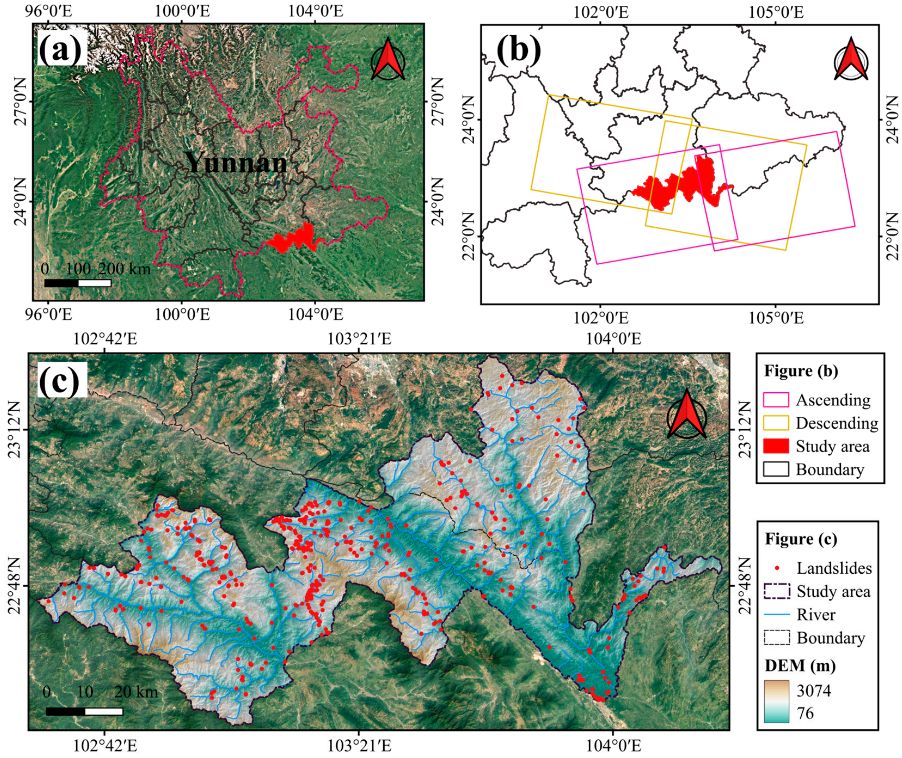

Figure 1. Geographical setting and spatial extent of the research area: (**a**) location of the study area in Yunnan Province, China; (**b**) coverage of Sentinel-1 satellite imagery; (**c**) geographic scope of the study region and distribution of recorded landslides.

2.2. Landslide Inventory Map

A total of 514 historical landslide sites are located within the landslide disaster warning demonstration area in Honghe Prefecture, covering a combined area of 8.569 km^2, as shown in Figure 1c. Relevant landslide data can be obtained from the official website of the Yunnan Provincial Department of Natural Resources: http://dnr.yn.gov.cn/ (accessed on 11 December 2024). Among these, the largest landslide measures 1.238 km^2, while the smallest covers only 40 m^2. Landslides are categorized by volume, resulting in 395 small-scale landslides (approximately 76.85%), 99 medium-scale landslides (about 19.26%), 18 large-scale landslides (around 3.50%), and 2 extra-large landslides (about 0.39%). Most landslide events in the region are relatively small and tend to occur along valley slopes.

2.3. Landslide Conditioning Factors

Landslides typically result from the combined effect of multiple LCFs. Carefully selecting relevant LCFs is crucial to improve the reliability of landslide susceptibility models [39]. In this research, based on previous studies and expert knowledge, we chose 15 static factors and 2 dynamic factors. As shown in Table 1 and Figure 2, the 15 static factors in this study include five categories of influencing elements: topography and landforms, geological foundations, vegetation cover, hydrometeorological conditions, and human activities. Based on the environmental features identified through field investigation, the chosen static LCFs include elevation, slope, aspect, plan curvature (PLC), profile curvature (PRC), topographic wetness index (TWI), stream power index (SPI), distance to fault (DTFA), lithology, distance to river (DTRI), distance to road (DTRO), land use/land cover (LULC), precipitation, normalized difference vegetation index (NDVI), and kernel density of points of interest (POI). Specifically, DTFA was divided into five intervals: 0–500 m, 500–1000 m, 1000–1500 m, 1500–2000 m, and over 2000 m. Lithology was categorized into nine types: limestone, pyroxenite, amphibolite, basic rock, gabbro, diabase, granite, quartzite, and muscovite. DTRI was grouped into six classes: 0–300 m, 300–600 m, 600–900 m, 900–1200 m, 1200–1500 m, and over 1500 m. DTRO was classified into five categories: 0–250 m, 250–750 m, 750–1250 m, 1250–2000 m, and over 2000 m. LULC was divided into seven categories: tree cover, shrubland, grassland, cropland, built-up areas, bare vegetation, and permanent water bodies. The remaining continuous variables were classified using the natural breaks method.

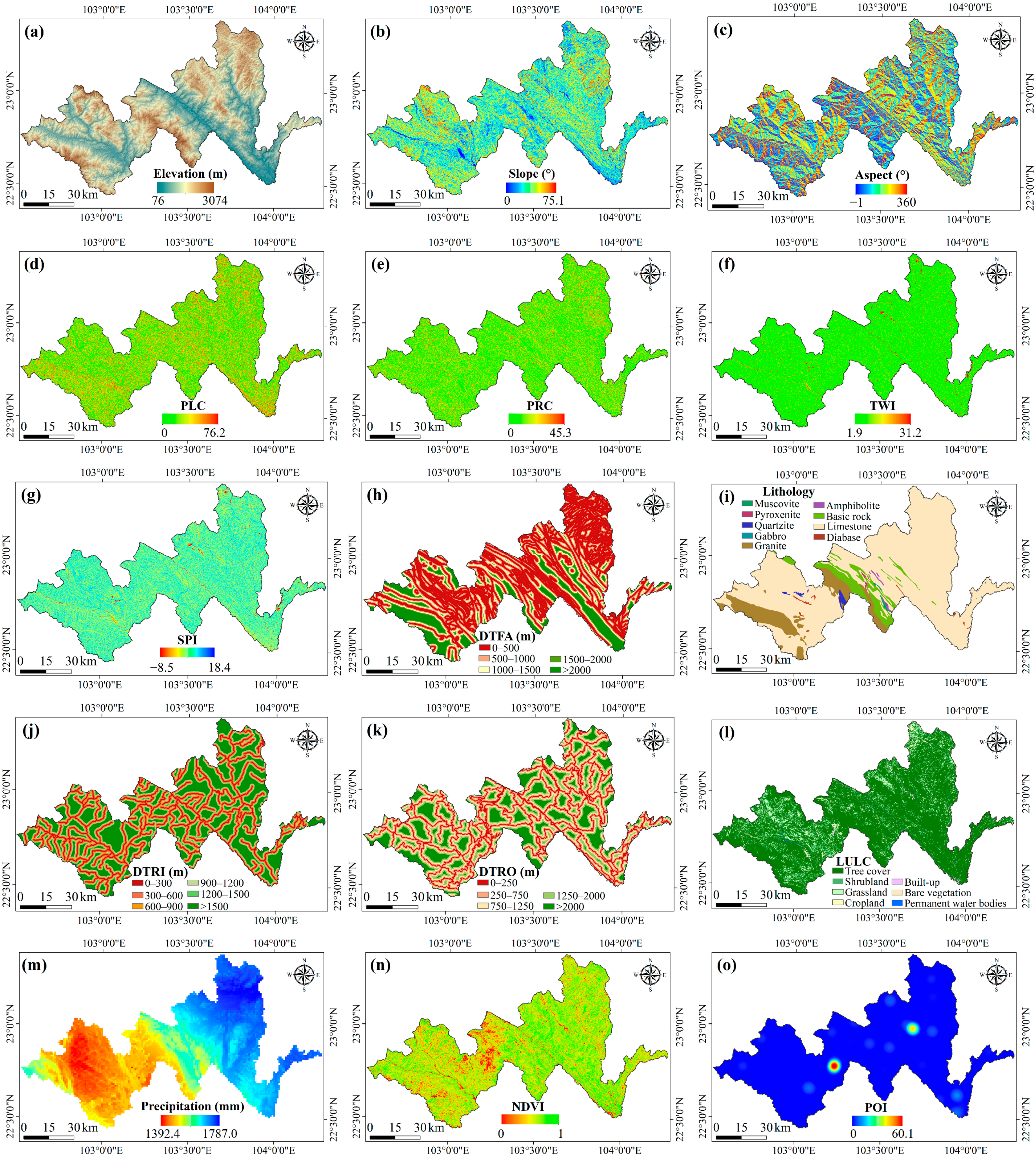

Figure 2. Thematic map of LCFs. (**a**) Elevation; (**b**) slope; (**c**) aspect; (**d**) PLC; (**e**) PRC; (**f**) TWI; (**g**) SPI; (**h**) DTFA; (**i**) lithology; (**j**) DTRI; (**k**) DTRO; (**l**) LULC; (**m**) precipitation; (**n**) NDVI; (**o**) POI kernel density.

Table 1. Detailed information on LCFs.

LCFs	Values	Data Type	Data Sources	Resolution
Elevation (m)	[76, 3074]	Continuous	https://earthexplorer.usgs.gov/, accessed on 11 December 2024	30 m
Slope (°)	[0, 75.1]	Continuous	Generated using elevation	30 m
Aspect (°)	[−1, 360]	Continuous	Generated using elevation	30 m
PLC	[0, 76.2]	Continuous	Generated using elevation	30 m
PRC	[0, 45.3]	Continuous	Generated using elevation	30 m
TWI	[1.9, 31.2]	Continuous	Generated using elevation	30 m
SPI	[−8.5, 18.4]	Continuous	Generated using elevation	30 m
DTFA (m)	5 types	Discrete	http://dnr.yn.gov.cn/, accessed on 11 December 2024	30 m
Lithology	9 types	Discrete	http://dnr.yn.gov.cn/, accessed on 15 December 2024	30 m
DTRI (m)	6 types	Discrete	https://www.webmap.cn/, accessed on 11 December 2024	30 m
DTRO (m)	5 types	Discrete	https://www.webmap.cn/, accessed on 11 December 2024	30 m
LULC	7 types	Discrete	https://esa-worldcover.org/, accessed on 11 December 2024	10 m
Precipitation (mm)	[1392.4, 1787.0]	Continuous	http://www.geodata.cn/, accessed on 15 December 2024	1 km
NDVI	[0, 1]	Continuous	https://www.resdc.cn/, accessed on 11 December 2024	30 m
POI kernel density	[0, 60.1]	Continuous	https://download.geofabrik.de/, accessed on 19 December 2024	30 m

The two dynamic LCFs are the ascending (ASC) and descending (DES) deformation rates derived from InSAR technology. In the early stages of a landslide, the internal structure of the rock and soil mass undergoes slight displacements and stress variations caused by factors such as gravity and pore water pressure. The gradual accumulation of deformation ultimately reduces slope stability [40]. Therefore, surface deformation is a critical metric for landslide monitoring. InSAR enables the collection of high-temporal and high-spatial resolution surface deformation fields, which directly reflect internal stress conditions within the rock and soil mass. This study utilized SAR data acquired from Sentinel-1A, operated by the European Space Agency (ESA). The dataset contains 182 ascending images (captured between 2 January 2019 and 29 December 2021) and 154 descending images (captured between 4 January 2019 and 19 December 2021). Figure 1b illustrates the spatial coverage, while Table 2 lists the corresponding imaging parameters in detail. In this study, both ASC and DES were combined with static LCFs as input features for the LSA model. All factors went through a consistent preprocessing process and then classification and frequency ratio (FR) analysis to aid in modeling, with the goal of improving the model's ability to respond to dynamic deformation features related to landslide processes.

Table 2. Detailed information on Sentinel-1A.

Basic Parameters	**Sentinel-1A**
Data sources	https://search.asf.alaska.edu/, accessed on 20 December 2024
Orbital direction	Ascending/Descending
Spatial resolution (m)	5 × 20
Incidence angle (°)	39.14/39.38
Polarization mode	VV
Band	C
Beam mode	IW
Radar wavelength (cm)	5.6
Acquisition time	2 January 2019 to 29 December 2021; 4 January 2019 to 19 December 2021
Number of images	182/154

Prior to model construction, a series of preprocessing steps were performed on the selected LCFs to ensure their spatial consistency and suitability for analysis. The preprocessing mainly involved unifying coordinate systems and resampling spatial resolution. Coordinate unification consisted of projecting all geospatial datasets into a common coordinate reference system to enable accurate spatial alignment and seamless overlay of data from different sources. Given the use of a 1:50,000 topographic mapping scale in this study and following the empirical formula for grid size proposed by Li and Zhou [41], a grid cell resolution of 30 m × 30 m was adopted. To address the resolution discrepancies among various datasets, all LCFs were resampled to a uniform 30 m resolution using bilinear interpolation. This standardization ensured consistency in the number of rows and columns across all raster layers, thereby facilitating the subsequent spatial analyses.

3. Methodology

The spatial variability of geographic and environmental factors—such as topography, geology, vegetation cover, rainfall, and human activities—results in regional differences in landslide-triggering mechanisms and the intensity of LCFs, thereby giving rise to pronounced spatial heterogeneity. Considering this heterogeneity not only enhances the scientific rigor and regional applicability of the assessment results but also supports the development of more targeted disaster prevention and mitigation strategies [42]. In this study, a novel SHP method based on t-SNE-ISO is proposed to achieve objective zonation of the study area, thereby improving the model's responsiveness to regional variations. Meanwhile, to address the issues of feature redundancy and interference commonly encountered in full-area modeling, a Pearson–GeoDetector (PG)-based feature selection strategy is introduced to optimize feature combinations and enhance the accuracy and robustness of the model. The overall technical workflow of this study is illustrated in Figure 3 and consists of the following four stages:

Stage 1 aims to quantitatively analyze the spatial correlation between LCFs and landslide events, establishing a basis for future modeling. Specifically, 15 static LCFs were collected and preprocessed and then discretized and weighted using the frequency ratio (FR) method to construct the static LCFs dataset.

Stage 2 focuses on incorporating dynamic LCFs to compensate for the limited capability of static factors in capturing the preparatory phase of landslides, thereby better revealing the spatiotemporal evolution of landslide processes. InSAR technology was employed to process Sentinel-1A imagery and derive annual average surface deformation rates in both ascending and descending orbits, which were used as dynamic LCFs.

Stage 3 addresses spatial heterogeneity by introducing the t-SNE-ISO approach and mitigates the limitations of traditional unidimensional feature selection by implementing the PG feature selection strategy. The proposed t-SNE-ISO method first applies t-SNE to reduce the dimensionality of the combined LCFs and landslide point data, preserving local structural features. The reduced-dimension data are then clustered using the ISO clustering algorithm, followed by the generation of Voronoi polygons to delineate spatially heterogeneous subregions. Concurrently, the PG strategy combines Pearson correlation analysis and GeoDetector at both global and local scales to identify the optimal feature subset.

Stage 4 constructs and evaluates a series of stacking EL models for LSM, integrating spatial heterogeneity and feature selection. A stacking framework was developed by combining CNN, DNN, and MLP as base learners. Four models—stacking, F-stacking, H-stacking, and HF-stacking—were developed, reflecting various combinations of SHP and feature selection. The models were comprehensively evaluated and compared using seven evaluation metrics (EMs), including AUC, OA, and F1 score.

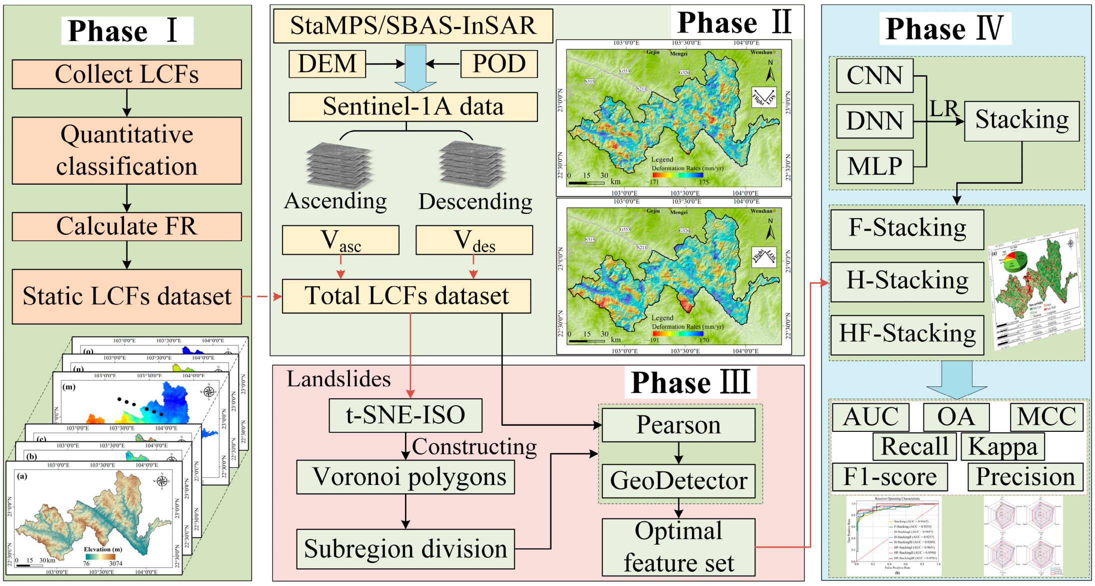

Figure 3. The main workflow framework of this study.

3.1. StaMPS/SBAS-InSAR

Initially established by Hooper et al. in 2004, the Stanford method for persistent scatterers (StaMPS) technique represents a significant milestone in the evolution of multi-temporal InSAR methodologies [43]. This method is compatible with both persistent scatterer interferometry (PSI) based on a single master image and small baseline subset interferometry (SBAS-InSAR) based on multiple master images, thereby significantly enhancing surface deformation monitoring capabilities in areas characterized by complex terrain. In this study, the StaMPS/SBAS-InSAR technique is employed to derive ground deformation information within the study area. The core processing workflow of the StaMPS/SBAS-InSAR technique mainly comprises four key steps: (1) generating a stack of differential interferograms based on predefined temporal and spatial baseline thresholds; (2) selecting slowly decorrelating filtered phase (SDFP) points using a coherence thresholding method; (3) constructing a Delaunay triangulation network to enable phase unwrapping; and (4) applying spatiotemporal filtering techniques to isolate and remove topographic, atmospheric, and orbital errors, thereby yielding accurate surface deformation measurements.

To address topographic phase distortion, this study utilizes a digital elevation model (DEM) with a 30 m spatial resolution, sourced from the Shuttle Radar Topography Mission (SRTM) and made publicly available by NASA. Additionally, precise orbit determination (POD) information released by the ESA is used to correct systematic errors in the interferometric baselines. The complete StaMPS/SBAS-InSAR processing workflow is summarized in Figure 4.

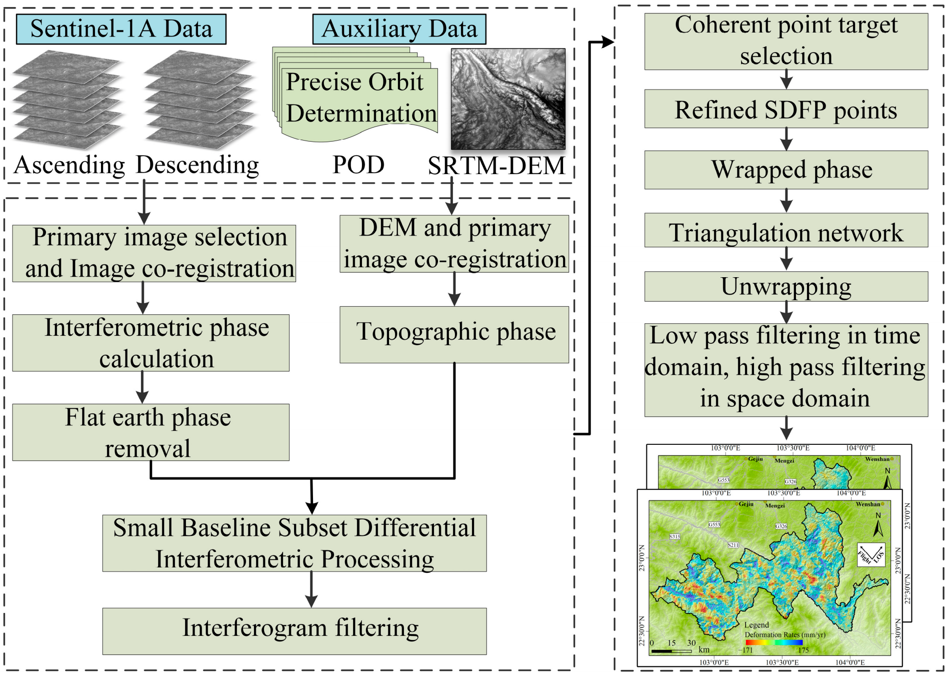

Figure 4. Processing workflow of StaMPS/SBAS-InSAR.

The study employed two software packages—Sentinel-1 Interferometric Processor (S1IP) and the StaMPS v3.3b1—to process a total of 182 ascending and 154 descending Sentinel-1 SAR images using the StaMPS/SBAS-InSAR technique. S1IP, developed by the Radar Imaging Geodesy Group at Peking University, is an InSAR processing tool known for its high efficiency in interferogram co-registration and image filtering. StaMPS v3.3b1 is an open-source software widely used for time-series InSAR analysis, particularly effective in processing long-term datasets of phase-stable scatterers. Following a series of adjustments and optimizations, a temporal baseline limit of 37 days and a spatial baseline constraint of 150 m were adopted, based on coherence levels observed during interferometric analysis. Interferograms exhibiting low coherence or significant errors were discarded, resulting in 531 valid ascending interferograms and 428 valid descending interferograms. A coherence threshold of 0.2 was applied, enabling the successful extraction of 449,344 SDFP points from the ascending data and 463,071 points from the descending data. To improve the accuracy of phase unwrapping, the extracted SDFP points were processed within an integrated environment using StaMPS v3.3b1 and MATLAB 2018a on an Ubuntu 14.04 system. A three-dimensional (3D) phase unwrapping algorithm based on spatiotemporal joint constraints was implemented to effectively address abrupt phase gradients in steep terrain areas.

3.2. Frequency Ratio Method

Due to differences in dimensions and value ranges among the LCFs, which may affect the performance of the model, the frequency ratio (FR) method was adopted to eliminate the imbalance among the LCFs and simultaneously employed to derive negative samples for training purposes. FR values for each classified LCF were calculated using Equation (1), and subsequently, the FR values across the entire study area were derived by combining the LCF raster data. Areas with low FR values were randomly sampled to obtain a non-landslide sample set equal in size to the landslide sample set. To facilitate model training, the compiled dataset was divided into training and validation subsets using a 70% to 30% allocation.

$$FR = \frac{N_{i0}/N_i}{S_0/S} \tag{1}$$

where N_{i0} denotes the extent of landslide occurrences within the ith interval of the LCFs; N_i denotes the total historical landslide area within the research region; S_0 refers to the extent of the ith attribute interval of the LCFs; and S signifies the total area of the study region.

3.3. Spatial Heterogeneity Partitioning Method

This study proposes a t-SNE-ISO-based SHP method to mitigate the adverse effects of spatial heterogeneity on the construction of LSA models. In this method, the Calinski–Harabasz (CH) index is used to determine the optimal distance metric and the number of clusters in the ISO clustering analysis. The distance metrics considered include Euclidean distance, Manhattan distance, and cosine distance. Leveraging the nonlinear dimensionality reduction capabilities of the t-SNE algorithm, high-dimensional and complex LCFs data are mapped to a lower-dimensional space, preserving their intrinsic structure and local feature information as much as possible during the process. Building upon this, the ISO algorithm is introduced to cluster the dimensionality-reduced samples, uncovering potential distribution patterns of landslide points in the attribute space. The clustering results are further used to generate Voronoi polygons, enabling SHP of the study area.

3.3.1. t-SNE Algorithm

t-SNE is a nonlinear technique for dimensionality reduction that transforms high-dimensional data into a lower-dimensional representation by preserving the relative pairwise similarity structure between the input and embedded spaces [44]. The algorithm achieves this by employing a probabilistic model that aligns the similarity distributions in both spaces, optimizing the embedding through the minimization of Kullback–Leibler (K-L) divergence. In the original high-dimensional space, similarities among data points are represented as conditional probabilities computed based on a Gaussian kernel. For each data point x_i in the high-dimensional space, the conditional probability $p_{j|i}$, reflecting its similarity to a neighboring point x_j, is computed as shown in Equation (2), where σ_i denotes the standard deviation of the Gaussian kernel centered at x_i.

$$p_{j|i} = \frac{\exp(-\|x_i - x_j\|^2/(2\sigma_i^2))}{\sum\limits_{k \neq i} \exp(-\|x_i - x_k\|^2/(2\sigma_i^2))} \tag{2}$$

In the embedded low-dimensional space, once the high-dimensional inputs x_i and x_j are transformed into their projections y_i and y_j, the conditional probability $q_{j|i}$, describing the likelihood of y_j appearing in the neighborhood of y_i, is formulated as

$$q_{j|i} = \frac{\exp(-\|y_i - y_j\|^2)}{\sum\limits_{k \neq i} \exp(-\|y_i - y_k\|^2)} \tag{3}$$

Finally, the consistency between the low-dimensional distribution Q_i and the high-dimensional distribution P_i is assessed using K-L divergence. Dimensionality reduction is achieved by minimizing this K-L divergence. The objective function and the gradient calculation formulas are provided in Equations (4) and (5).

$$C = \sum_i KL(P_i \| Q_i) = \sum_i \sum_j p_{j|i} \log \frac{p_{j|i}}{q_{j|i}} \tag{4}$$

$$\frac{\partial C}{\partial y_i} = 2\sum_j (p_{j|i} - q_{j|i} + p_{i|j} - q_{i|j})(y_i - y_j) \tag{5}$$

In this study, the t-SNE algorithm was implemented using the scikit-learn library in Python 3.7. Given the sensitivity of t-SNE to hyperparameters—particularly perplexity and learning rate—we conducted a grid search over perplexity values of 10, 20, 30, 40, and 50, as well as learning rates of 100, 200, and 300. The resulting two-dimensional embeddings were visually assessed for cluster boundary clarity and inter-class separability. Based on this evaluation, a perplexity of 30 and a learning rate of 200 were selected as the optimal parameters and subsequently applied in the downstream modeling analyses.

3.3.2. ISO Algorithm

ISO clustering is an iterative self-organizing data analysis technique widely utilized in unsupervised learning for clustering analysis [45]. The fundamental concept involves dynamically adjusting cluster centers by iteratively optimizing and minimizing intra-cluster variance, thereby partitioning the data into several homogeneous categories. During each iteration, the algorithm assigns sample x_i to its closest cluster center according to a predefined distance metric. Subsequently, cluster centroids are recalculated as the average of all members within the respective clusters. This procedure repeats until convergence criteria are satisfied. Through multiple trials and parameter tuning, the key parameters were ultimately set as follows: LeastSampleNum to 10, StdThred to 0.5, and LeastCenterDist to 2. The clustering performance was comprehensively evaluated by considering the CH index, intra-cluster compactness, inter-cluster separability, and the visualization of clusters in two-dimensional space. This multi-faceted assessment ensured that the clustering results were statistically robust as well as spatially coherent and stable.

3.4. Feature Selection Method

The mechanisms driving landslide development and their triggering factors vary significantly. Incorporating all features indiscriminately into models may compromise data validity and negatively impact model accuracy. To ensure feature independence and enhance model robustness, this study adopts the PG feature selection strategy to determine an optimal feature subset. The analysis begins by computing the Pearson correlation coefficient (r) to assess linear relationships among global features. If r exceeds a threshold of 0.45, that feature is removed; otherwise, it is retained. This threshold of 0.45 represents a balanced cutoff value chosen based on the correlation distribution of LCFs in the study area and commonly adopted empirical ranges reported in the literature [7,35]. The aim is to reduce feature redundancy while preserving as much useful information as possible. The following expression illustrates the computation procedure.

$$r = \frac{\sum\limits_{i=1}^{n} (x_i - \overline{x})(y_i - \overline{y})}{\sqrt{\sum\limits_{i=1}^{n} (x_i - \overline{x})^2} \cdot \sqrt{\sum\limits_{i=1}^{n} (y_i - \overline{y})^2}} \tag{6}$$

where x_i and y_i represent the observed values of two feature factors, $\overline{x}$ and $\overline{y}$ denote the mean values of the samples for x and y, respectively. The n is the sample size.

Based on the feature set refined by redundancy elimination, the factor detector of GeoDetector was further employed to identify the factors with significant explanatory power for landslide distribution, thereby enabling the construction of the optimal feature subset. The q statistic from factor detection quantifies how effectively a feature variable X accounts for the spatial variation of landslide susceptibility Y, ranging from 0 to 1. Higher q values reflect greater explanatory strength of X regarding Y [46,47]. The calculation formula is presented as Equation (7).

$$q = 1 - \frac{\sum_{h=1}^{L} N_h \sigma_h^2}{N\sigma^2} \tag{7}$$

where h = 1, 2, 3, . . ., L represents the stratification levels of feature factor X. N denotes the total sample size, while N_h indicates the sample size within the hth stratification level. σ^2 denotes the overall variance of the dependent variable Y, while σ_h^2 reflects the variance of Y within the hth stratified subgroup.

3.5. Deep Learning Models

To enhance the robustness and predictive performance of LSA models, this study incorporates three representative deep learning models—CNN, DNN, and MLP—as base learners within the stacking ensemble framework. These models exhibit distinct strengths in feature extraction and nonlinear modeling: CNN excels at capturing local spatial features, DNN is effective for handling high-dimensional and complex data, and MLP demonstrates strong flexibility in architecture and fitting capability. By integrating these models as base learners, the ensemble effectively leverages multi-dimensional information, thereby improving overall predictive performance and adaptability to spatial heterogeneity. During model training, the three aforementioned DL models were optimized using a grid search strategy over a predefined hyperparameter space. The learning rate was varied across five orders of magnitude, ranging from 10^{-1} to 10^{-5}. The number of training epochs was set between 100 and 200 in increments of 20, while the batch size was tested at four levels: 32, 64, 128, and 256. Each candidate configuration was evaluated based on its performance on the validation set, using the area under the receiver operating characteristic curve (AUC) and F1 score as the primary evaluation criteria. The combination yielding the best classification performance was selected for subsequent modeling and prediction tasks.

3.5.1. CNN Model

CNN, originally introduced by LeCun et al. [48], was first applied to address handwritten digit classification problems in the context of DL. The convolution operation effectively extracts features from the data, leading to widespread applications in fields such as computer vision [49]. Geographic spatial data contain rich feature information, and the convolutional layers of CNN are adept at capturing spatial correlations and local patterns. This capability grants CNN a unique advantage in the LSA [50–52].

The framework of the CNN model is depicted in Figure 5. A feature vector of dimensions 17 × 1, containing the LCFs, is initially passed to the input layer of the network. Through convolution operations performed by convolutional kernels, the network accomplishes the extraction and learning of spatial and feature dimension information. To mitigate the risk of model overfitting, pooling layers aggregate neighboring pixels in the feature space, retaining essential features while reducing their dimensionality [53]. After the convolutional and pooling operations, the network effectively extracts features to create a landslide feature map. A flattening operation is then applied to reshape the extracted landslide feature map into a one-dimensional vector, which is subsequently passed to the fully connected (FC) layer for further processing. The FC layer applies nonlinear transformations to the extracted features, capturing the relationships between them. Ultimately, these features are mapped to a 0–1 output space using a sigmoid activation function, enabling landslide susceptibility prediction. After multiple rounds of training and parameter tuning, the final model configuration is determined with a batch size of 128, 200 epochs, and a learning rate of 1×10^{-5}.

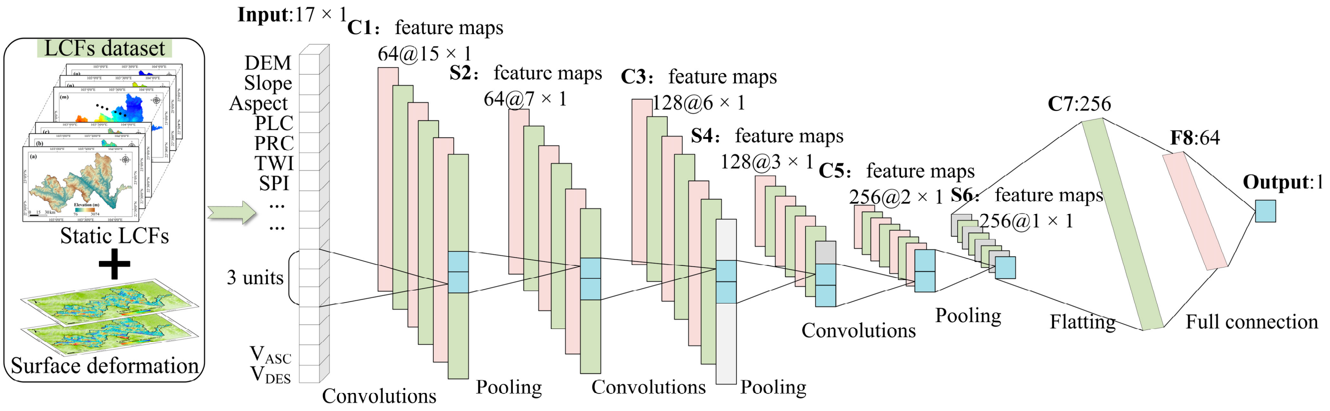

Figure 5. Structure diagram of the CNN.

3.5.2. DNN Model

DNN is a DL algorithm introduced by Hinton et al. [54] that is widely utilized in LSA due to its effectiveness in handling nonlinear problems [55–57]. As shown in Figure 6, the LCFs serve as the input layer. At this stage, the network assigns an initial weight W and bias b, and layer-by-layer computations are performed in the hidden layers according to Equations (8)–(10).

$$Z^{(1)} = W^{(1)}x + b^{(1)} \tag{8}$$

$$a^{(i)} = \sigma(Z^{(i)}) \tag{9}$$

$$y = W^{(i)}a^{(i-1)} + b^{(i)} \tag{10}$$

where x represents the input samples, denoted as $(x_1, x_2, \ldots, x_n)$, where n is the number of features; Z represents the output results, expressed as $(Z_1{}^{(\mathrm{i})}, Z_2{}^{(\mathrm{i})}, \ldots, Z_{16}{}^{(\mathrm{i})})$, with i indicating the layer number in the hidden layers and with the four hidden layers containing 16, 64, 128, and 16 neurons, respectively; a denotes the input values for the next layer of the network; σ signifies the activation function. ReLU is adopted in the hidden layers to embed non-linearity, while the sigmoid function is applied in the output layer to constrain outputs to the [0, 1] range. y signifies the predicted probability of landslide susceptibility. This study employs cross-entropy as the loss function and utilizes the Adam algorithm for optimization.

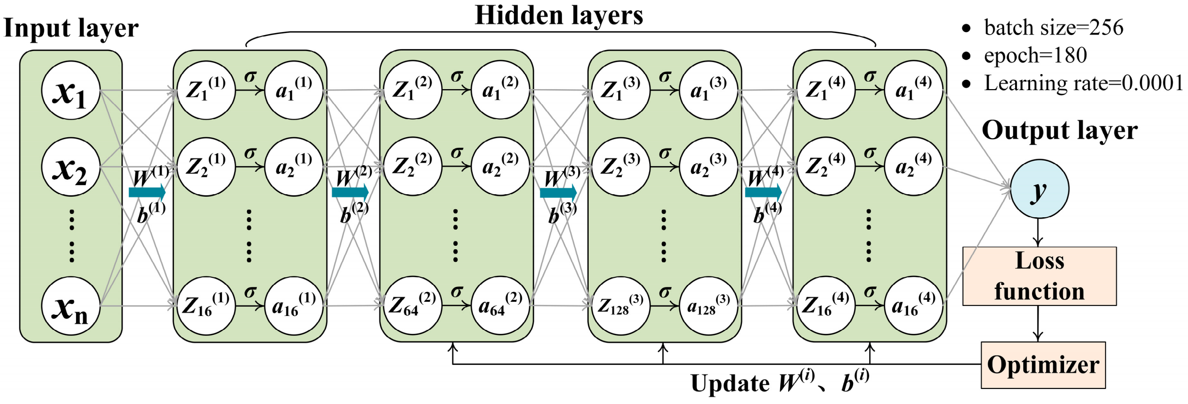

Figure 6. Structure diagram of the DNN.

3.5.3. MLP Model

MLP refers to a feedforward neural model composed of multiple layers, where parameter updates are performed through a unidirectional error backpropagation process [58]. A core advantage of this model is its ability to effectively establish mapping relationships in feature space through hierarchical nonlinear transformations, resulting in strong fitting capabilities [59]. Following multiple rounds of training and hyperparameter tuning, the MLP model constructed in this study was configured with three hidden layers of sizes 2, 16, and 32; a batch size of 128; 160 epochs; and a learning rate of 1×10^{-4}.

3.6. Stacking Ensemble Learning

Stacking is a hierarchical ensemble learning strategy that combines the outputs of multiple base learners as input features for a higher-level meta-model, which produces the final prediction results. This approach has the potential to improve predictive performance, mitigate overfitting, and increase the model's robustness in processing complex data [60]. The specific framework is illustrated in Figure 7. In this research, CNN, DNN, and MLP are selected as the base models, and the dataset is partitioned into five segments using a five-fold cross-validation approach. Four segments function as the training sets for the base models, while the rest of the segments are used as the cross-validation set. The prediction outputs of the base models are further aggregated as new landslide-related features, which are then fed into a logistic regression (LR) model serving as the meta-learner to generate the final prediction. Owing to its simple structure, low variance, and strong generalization ability, LR has been widely employed in stacking architectures to effectively integrate base learners' outputs and reduce the risk of overfitting [61].

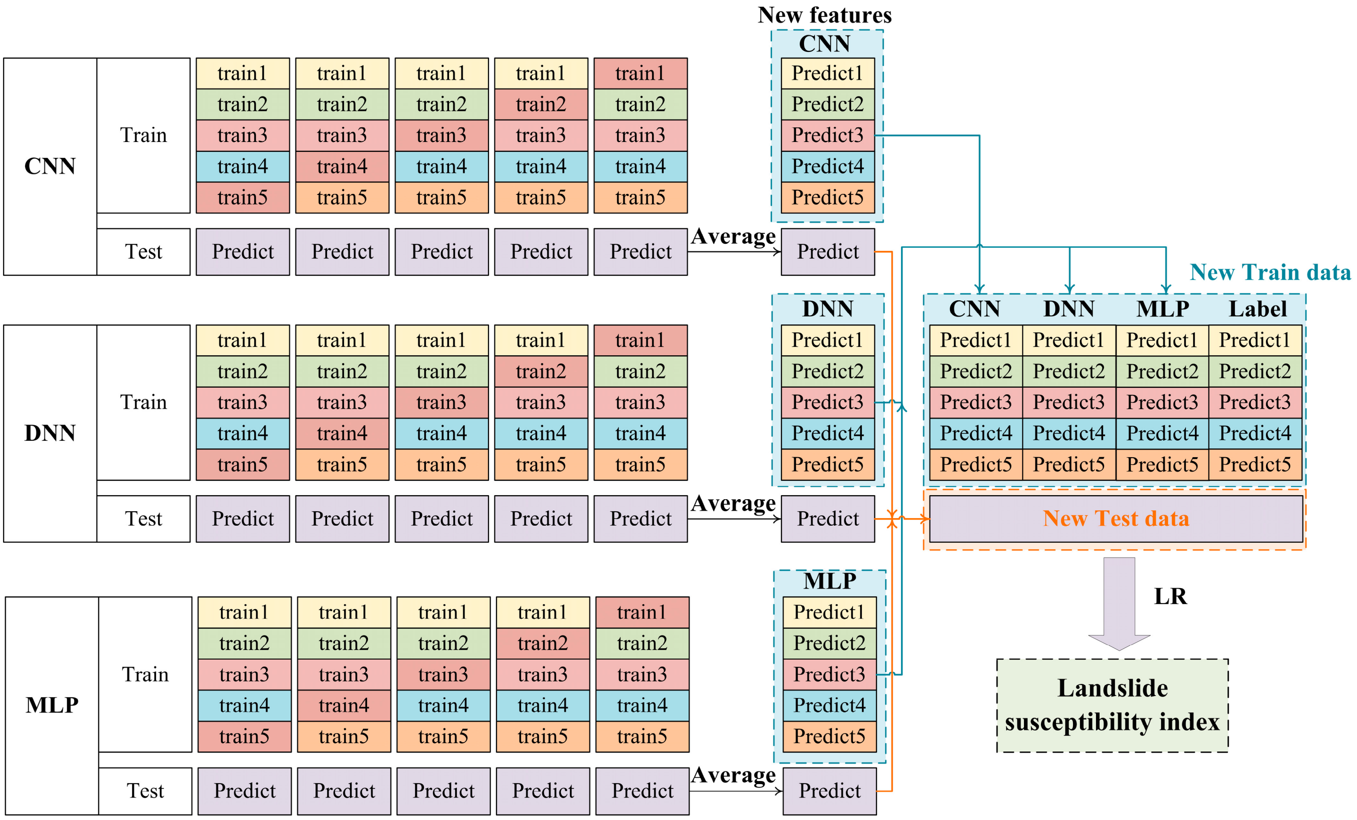

Figure 7. Structure diagram of the stacking ensemble learning model.

3.7. Model Evaluation Metrics

The EMs utilized in this study include AUC, overall accuracy (OA), precision, recall, F1 score, Matthews correlation coefficient (MCC), and kappa coefficient. The corresponding calculation formulas are provided below.

$$\mathrm{OA} = \frac{\mathrm{TP} + \mathrm{TN}}{\mathrm{TP} + \mathrm{FN} + \mathrm{FP} + \mathrm{TN}} \tag{11}$$

$$\mathrm{Precision} = \frac{\mathrm{TP}}{\mathrm{TP} + \mathrm{FP}} \tag{12}$$

$$\mathrm{Recall} = \frac{\mathrm{TP}}{\mathrm{TP} + \mathrm{FN}} \tag{13}$$

$$\mathrm{F1} - \mathrm{score} = 2 \times \frac{\mathrm{Precision} \times \mathrm{Recall}}{\mathrm{Precision} + \mathrm{Recall}} \tag{14}$$

$$\mathrm{MCC} = \frac{\mathrm{TP} \times \mathrm{TN} - \mathrm{FP} \times \mathrm{FN}}{\sqrt{(\mathrm{TP} + \mathrm{FP})(\mathrm{TP} + \mathrm{FN})(\mathrm{TN} + \mathrm{FP})(\mathrm{TN} + \mathrm{FN})}} \tag{15}$$

$$\mathrm{Kappa} = \frac{\mathrm{OA} - \mathrm{Pe}}{1 - \mathrm{Pe}} \tag{16}$$

$$\mathrm{Pe} = \frac{(\mathrm{TP} + \mathrm{FN})(\mathrm{TP} + \mathrm{FP}) + (\mathrm{FP} + \mathrm{TN})(\mathrm{FN} + \mathrm{TN})}{(\mathrm{TP} + \mathrm{FP} + \mathrm{TN} + \mathrm{FN})^2} \tag{17}$$

In classification evaluation, the following notations are used: TP (true positives) refers to landslide instances correctly classified; TN (true negatives) denotes non-landslides correctly predicted; FP (false positives) corresponds to non-landslides misclassified as landslides; and FN (false negatives) indicates landslides that were incorrectly predicted as non-landslides. Metrics with values closer to 1 typically reflect stronger predictive performance. Among them, AUC is a key indicator widely used to assess the effectiveness of binary classification models. It is defined as the area under the receiver operating characteristic (ROC) curve plotted in a two-dimensional coordinate system, bounded by the curve and the coordinate axes. An AUC value approaching 1 signifies that the model possesses excellent discriminative ability [62]. In contrast, an AUC near 0.5 reflects limited discriminative power, implying that the model performs no better than random guessing in separating positive and negative samples.

4. Results

4.1. Dynamic Factors Results

To obtain continuous surface deformation rates across the study area, this study employed the ordinary Kriging interpolation method. Based on the assumption of spatial stationarity and utilizing an exponential variogram model, spatial interpolation was performed on the stable SDFP points extracted via StaMPS/SBAS-InSAR. This process yielded annual average deformation rate maps covering the entire study area, as shown in Figure 8, including both ascending and descending deformation rates. In the maps, positive values indicate surface uplift, while negative values denote subsidence. The results show that the ascending line-of-sight (LOS) deformation rates range from −171 to 175 mm/yr, with an average subsidence rate of 27.8 mm/yr. The descending LOS deformation rates range from −191 to 171 mm/yr, with an average subsidence rate of 39.1 mm/yr. These findings reveal significant spatial variability in surface deformation within the study area, with higher subsidence rates primarily concentrated in mountainous regions with dense terrain.

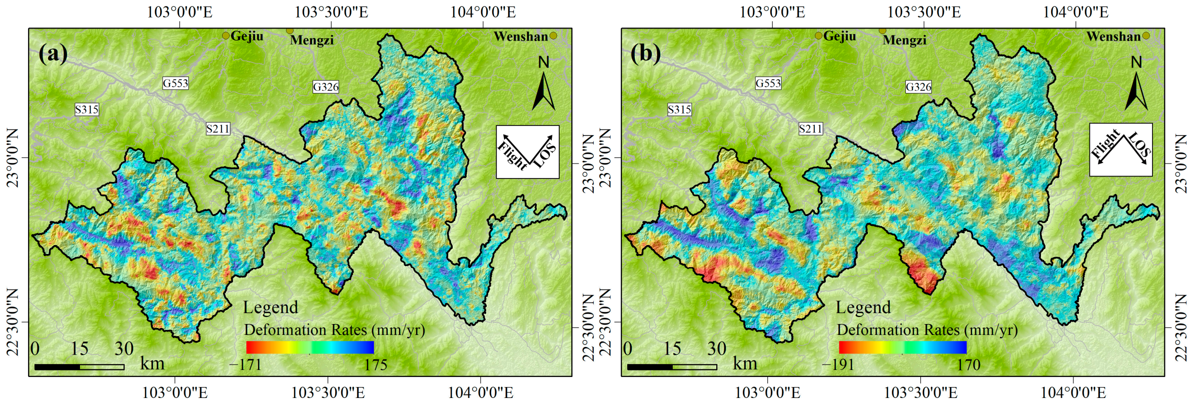

Figure 8. Average annual deformation rates in the research area: (**a**) ascending deformation; (**b**) descending deformation.

4.2. Spatial Heterogeneity Partitioning

To determine the optimal distance metric and number of clusters for the ISO clustering algorithm, this study evaluated the CH index under three distance measures: Euclidean, Manhattan, and cosine. The variation of CH scores with different cluster numbers is shown in Figure 9. As illustrated, the clustering performance was highest under the Euclidean distance, where the CH index peaked at 14.1 when the number of clusters was three. This indicates that Euclidean distance provides the greatest inter-cluster separability and intra-cluster compactness. The Manhattan distance ranked second, with a CH value of 10.3 when the number of clusters was four. In contrast, clustering performance under the cosine distance was significantly weaker, with a maximum CH value of only 1.2. Based on these comparisons, Euclidean distance was deemed most suitable for capturing the distribution characteristics of landslide samples in the t-SNE-reduced space, effectively distinguishing their differences in the LCFs attribute domain. Consequently, Euclidean distance was selected as the final distance metric, and the t-SNE-reduced landslide samples were clustered into three categories using the ISO clustering algorithm. The resulting SHP is presented in Figure 10, which clearly identifies three spatially heterogeneous subregions within the study area.

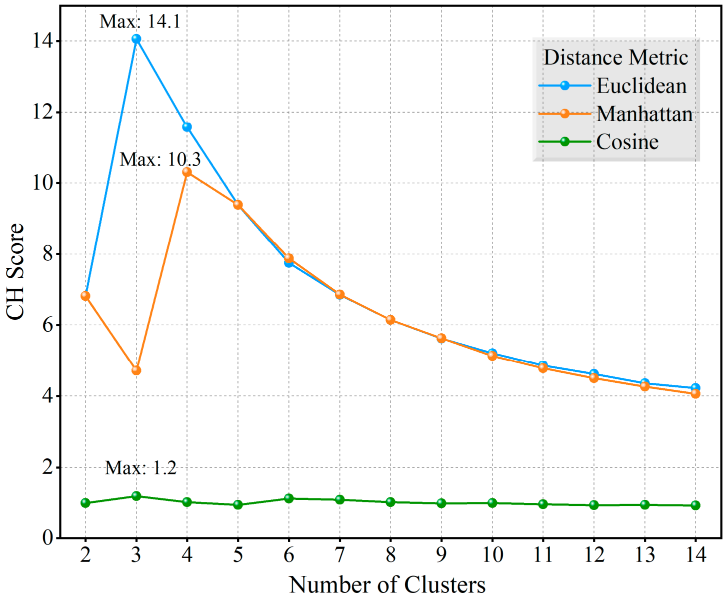

Figure 9. The CH values for different cluster counts under various distance metrics.

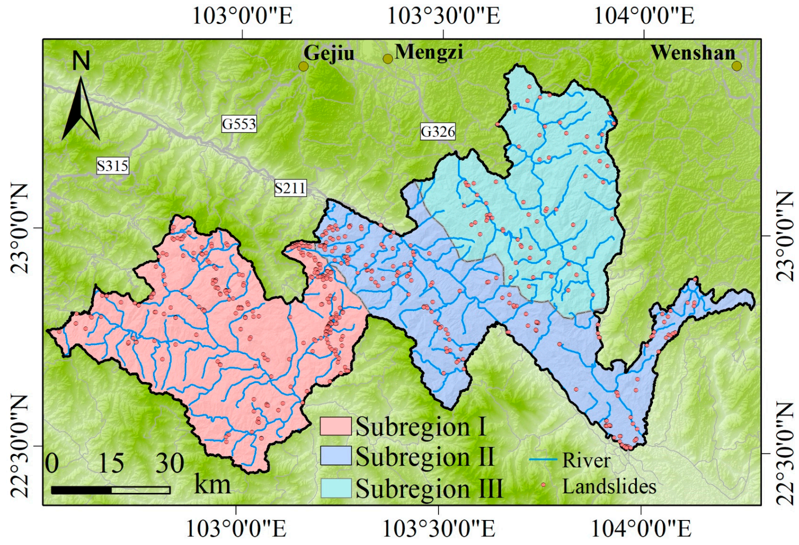

Figure 10. SHP results of the landslide disaster warning area.

4.3. Feature Selection

Figure 11 presents the Pearson correlation coefficients for the global LCFs. In the figure, red denotes a positive correlation, while blue signifies a negative correlation. The intensity of the colors corresponds to the strength of the correlations. The results indicate that the *r*-value between PLC and slope is −0.56, while the *r*-value between TWI and SPI is 0.45, both exceeding the threshold of 0.45. Notably, the correlation between TWI and slope reaches −0.41, suggesting a linear relationship. Consequently, this study excludes TWI and PLC from further analysis.

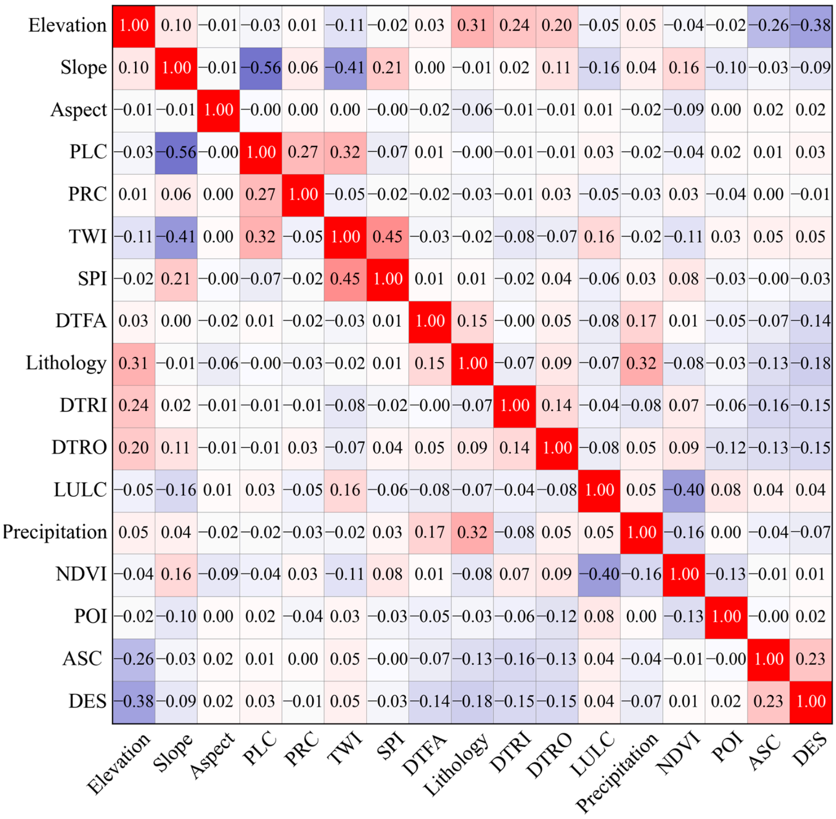

	Elevation	Slope	Aspect	PLC	PRC	TWI	SPI	DTFA	Lithology	DTRI	DTRO	LULC	Precipitation	NDVI	POI	ASC	DES
Elevation	1.00	0.10	−0.01	−0.03	0.01	−0.11	−0.02	0.03	0.31	0.24	0.20	−0.05	0.05	−0.04	−0.02	−0.26	−0.38
Slope	0.10	1.00	−0.01	−0.56	0.06	−0.41	0.21	0.00	−0.01	0.02	0.11	−0.16	0.04	0.16	−0.10	−0.03	−0.09
Aspect	−0.01	−0.01	1.00	−0.00	0.00	0.00	−0.00	−0.02	−0.06	−0.01	−0.01	0.01	−0.02	−0.09	0.00	0.02	0.02
PLC	−0.03	−0.56	−0.00	1.00	0.27	0.32	−0.07	0.01	−0.00	−0.01	−0.01	0.03	−0.02	−0.04	0.02	0.01	0.03
PRC	0.01	0.06	0.00	0.27	1.00	−0.05	−0.02	−0.02	−0.03	−0.01	0.03	−0.05	−0.03	0.03	−0.04	0.00	−0.01
TWI	−0.11	−0.41	0.00	0.32	−0.05	1.00	0.45	−0.03	−0.02	−0.08	−0.07	0.16	−0.02	−0.11	0.03	0.05	0.05
SPI	−0.02	0.21	−0.00	−0.07	−0.02	0.45	1.00	0.01	0.01	−0.02	0.04	−0.06	0.03	0.08	−0.03	−0.00	−0.03
DTFA	0.03	0.00	−0.02	0.01	−0.02	−0.03	0.01	1.00	0.15	−0.00	0.05	−0.08	0.17	0.01	−0.05	−0.07	−0.14
Lithology	0.31	−0.01	−0.06	−0.00	−0.03	−0.02	0.01	0.15	1.00	−0.07	0.09	−0.07	0.32	−0.08	−0.03	−0.13	−0.18
DTRI	0.24	0.02	−0.01	−0.01	−0.01	−0.08	−0.02	−0.00	−0.07	1.00	0.14	−0.04	−0.08	0.07	−0.06	−0.16	−0.15
DTRO	0.20	0.11	−0.01	−0.01	0.03	−0.07	0.04	0.05	0.09	0.14	1.00	−0.08	0.05	0.09	−0.12	−0.13	−0.15
LULC	−0.05	−0.16	0.01	0.03	−0.05	0.16	−0.06	−0.08	−0.07	−0.04	−0.08	1.00	0.05	−0.40	0.08	0.04	0.04
Precipitation	0.05	0.04	−0.02	−0.02	−0.03	−0.02	0.03	0.17	0.32	−0.08	0.05	0.05	1.00	−0.16	0.00	−0.04	−0.07
NDVI	−0.04	0.16	−0.09	−0.04	0.03	−0.11	0.08	0.01	−0.08	0.07	0.09	−0.40	−0.16	1.00	−0.13	−0.01	0.01
POI	−0.02	−0.10	0.00	0.02	−0.04	0.03	−0.03	−0.05	−0.03	−0.06	−0.12	0.08	0.00	−0.13	1.00	−0.00	0.02
ASC	−0.26	−0.03	0.02	0.01	0.00	0.05	−0.00	−0.07	−0.13	−0.16	−0.13	0.04	−0.04	−0.01	−0.00	1.00	0.23
DES	−0.38	−0.09	0.02	0.03	−0.01	0.05	−0.03	−0.14	−0.18	−0.15	−0.15	0.04	−0.07	0.01	0.02	0.23	1.00

Figure 11. Pearson correlation coefficients of LCFs.

GeoDetector was subsequently applied to evaluate how the remaining 15 LCFs affect the landslide events, considering both the entire study area and individual subregions, as illustrated in Figure 12. The results reveal notable differences in the q-values of LCFs across different regions; however, DTRO and the NDVI consistently emerge as the most influential factors at both the global scale and within each subregion. The impact of DTRO on landslide events is largely attributed to the interplay between anthropogenic engineering interventions and inherent geological conditions. Road construction alters local geological conditions and destabilizes slopes, thereby increasing landslide susceptibility. Generally, slopes situated nearer to roads exhibit a greater probability of landslide events. NDVI, which quantifies vegetation cover, indirectly reflects surface stability and regional hydrological conditions. As such, it serves as a key environmental indicator for landslide susceptibility. Dense vegetation contributes to slope stability by increasing soil cohesion through extensive root networks, thereby mitigating the potential for landslides. At the global level, DTRO exhibits the strongest explanatory capacity, indicated by a q-value of 40.2%. Notably, 75.9% of landslide events are located within 750 m of roadways. Regionally, DTRO remains the most influential factor in subregions I and II, with explanatory powers of 41.6% and 38.4%, respectively. In these subregions, 81% and 74% of landslides occur within the 750 m road buffer zone. Furthermore, the frequency of landslides decreases with increasing distance from roads. In subregion III, NDVI is identified as the most dominant factor, with a q-value of 37.5%. Landslides in this subregion predominantly occur in areas where NDVI values are below 0.7. Additionally, lithology fails to pass the 5% significance threshold in any subregion, indicating its limited explanatory power.

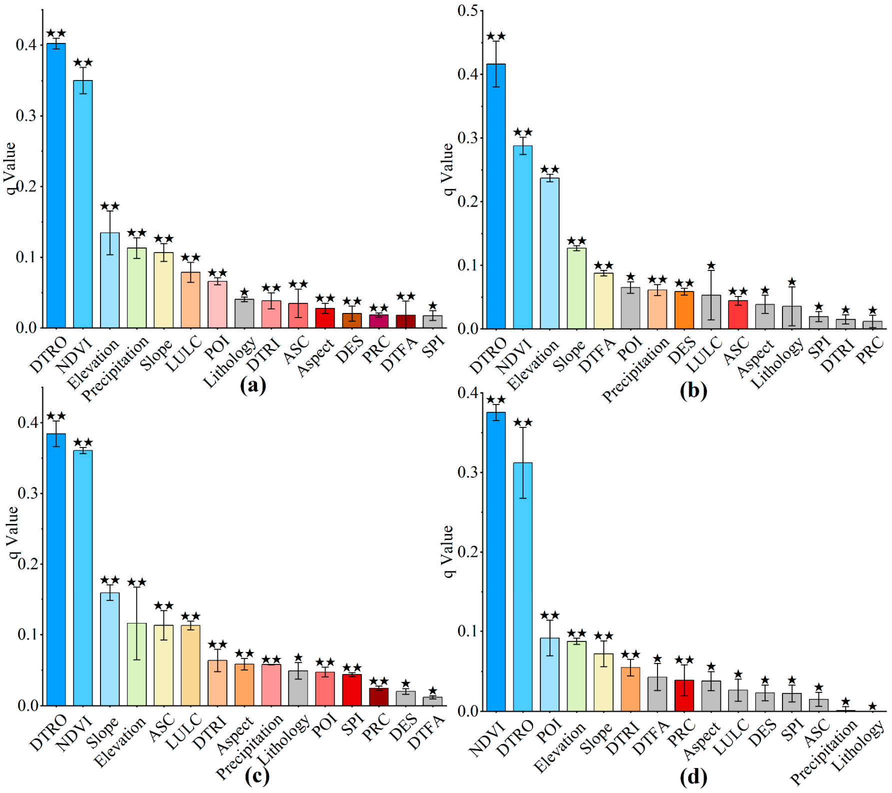

Figure 12. GeoDetector factor detection results. (**a**) Factor detector results for the entire study area; (**b**) factor detector results for subregion I; (**c**) factor detector results for subregion II; (**d**) factor detector results for subregion III. Note: A *p*-value below 0.05 is considered "significant" and is indicated with ★★, whereas a *p*-value that equals or exceeds 0.05 is deemed "not significant" and is represented with ★.

In summary, based on the results from GeoDetector, non-significant factors were excluded, while those with significant influence were retained as the optimal feature combinations for each region. The optimal feature combination for the global area includes DTRO, NDVI, elevation, precipitation, slope, LULC, POI, DTRI, ASC, aspect, DES, PRC, and DTFA. For subregion I, the optimal feature combination comprises DTRO, NDVI, elevation, slope, DTFA, precipitation, DES, and ASC. In subregion II, the optimal feature combination consists of DTRO, NDVI, slope, elevation, ASC, LULC, DTRI, aspect, precipitation, POI, SPI, and PRC. Lastly, in subregion III, the optimal feature combination includes NDVI, DTRO, POI, elevation, slope, DTRI, and PRC.

4.4. LSM Based on the Stacking Ensemble Model

To effectively mitigate the impact of spatial heterogeneity on LSA and to validate the effectiveness of feature selection strategies, this study employed CNN, DNN, and MLP as base learners, with LR serving as the meta-learner. Using stacking EL techniques, we constructed four comparative models: (1) global stacking model (without feature selection), (2) global F-stacking model (with feature selection only), (3) regional H-stacking model (with SHP only), and (4) regional HF-stacking model (with both SHP and feature selection). After building the ensemble models, we used LCFs as input variables to predict the probability of landslide susceptibility in the target area. A numerical landslide sensitivity index (LSI), scaled between 0 and 1, was assigned to each evaluation unit across the global study area, with larger values corresponding to higher landslide susceptibility. The LSI values were visualized using ArcGIS 10.7, where natural breaks classification was employed for dividing the data into five susceptibility categories: very low, low, moderate, high, and very high. Figure 13 displays the LSM predicted by the four models, all exhibiting similar distributions of susceptibility. To evaluate the computational feasibility of the proposed HF-stacking model, the training and evaluation processes were conducted on a standard workstation equipped with an Intel i5 processor and 32 GB of RAM. The entire modeling workflow required only a few minutes to complete without utilizing GPU acceleration, yet it achieved high predictive performance. These results demonstrate that the HF-stacking model offers favorable computational efficiency and resource adaptability while maintaining accuracy, making it well-suited for implementation in most conventional research and engineering settings.

The LSM results reveal that zones with very high LSI values are mostly distributed across the central region and follow significant transportation axes. Notably, the Jinhe Town area consistently exhibited high LSI values across all four models, indicating the highest likelihood of landslides. The geomorphological characteristics of this region feature significant topographic variation and a well-developed river network. Erosion along the slope edges by rivers leads to softening of the underlying materials, making them susceptible to collapse and reducing slope stability. Furthermore, the geological formation in this area is predominantly comprised of quartzite, which has high hardness and compressive strength, capable of supporting steep terrain. However, its brittleness means that under gravitational or tectonic stresses, the lower layers are prone to tensile failure, creating potential sliding surfaces that directly contribute to geological hazards.

Figure 14 presents the comparative ROC curves of various models based on five repeated experiments. Specifically, Figure 14a illustrates the average ROC curves of CNN, DNN, MLP, and the stacking ensemble model. Compared with other models, the stacking ensemble achieved notably better results, attaining an AUC of 91.67%, which indicates its superiority over individual DL models. Figure 14b illustrates the ROC curves for the improved stacking models that consider feature selection and SHP. The results indicate that all improved models achieved strong predictive capability, with AUC values exceeding

90%. Among them, the HF-stacking model yielded AUC values of 94.94%, 95.73%, and 97.02% across the three subregions, with a mean value of 95.90%. In contrast, the H-stacking model recorded AUC values of 94.41%, 91.94%, and 92.60% in the subregions, with an average AUC of 92.98%.

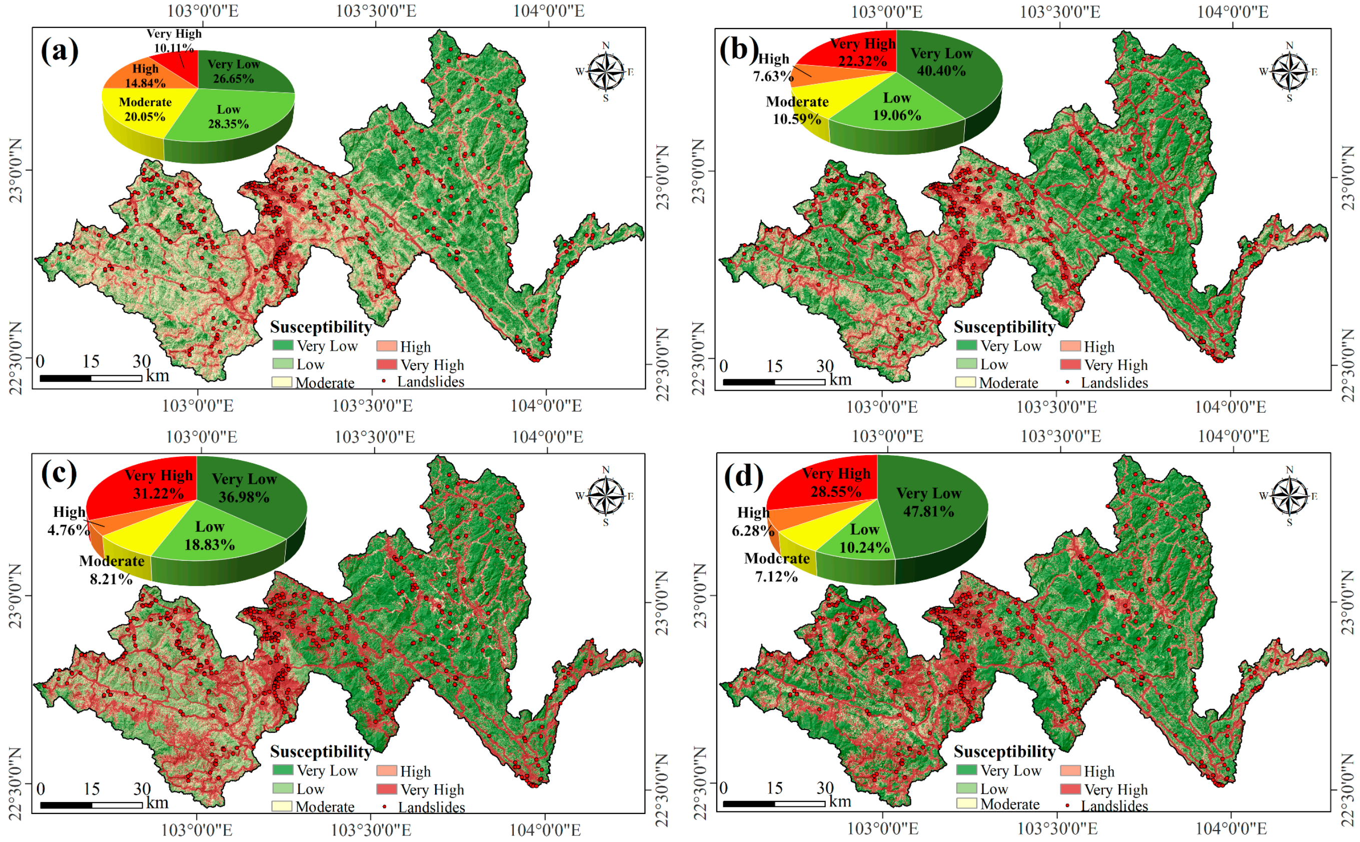

Figure 13. The results of LSM. (**a**) Stacking model; (**b**) F-stacking model; (**c**) H-stacking model; (**d**) HF-stacking model.

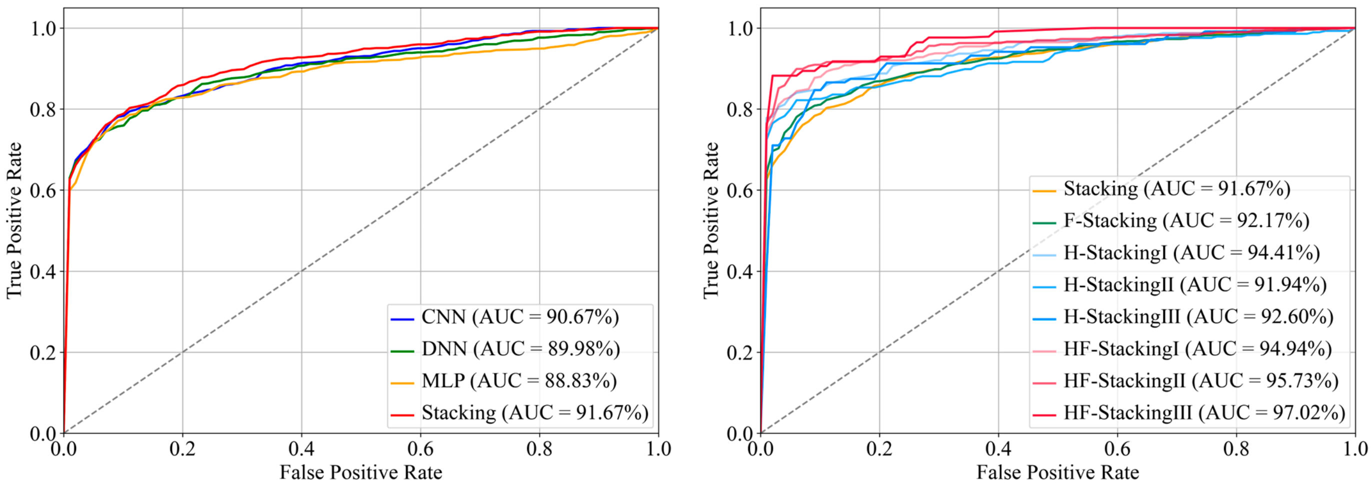

(**a**) (**b**)

Figure 14. The ROC curves of the models. (**a**) ROC curves and corresponding AUC values for CNN, DNN, MLP, and stacking models; (**b**) ROC curves and AUC values of stacking-based LSA models incorporating spatial heterogeneity partitioning (H) and feature selection (F) strategies.

Furthermore, the feature selection strategy improved the AUC of the F-stacking model by 0.50% compared to the stacking model. The implementation of SHP resulted in a 1.31% increase in the average AUC of the H-stacking model relative to the stacking model. The combined application of both strategies in the HF-stacking model achieved the most significant performance gain, with an average AUC increase of 4.23%. These experimental results demonstrate that both SHP and feature selection significantly enhance model performance, with their synergistic application yielding the best results.

5. Discussion

5.1. Evaluation of Model Accuracy and Predictive Capability

To accurately reflect the performance differences among the CNN, DNN, MLP, and stacking models, the four models were first evaluated in terms of predictive performance within the context of global conditions. The entire dataset was divided into training and validation sets in a 70:30 ratio, with the training set used for model fitting and the validation set employed for performance evaluation. To enhance the stability and reliability of the evaluation results, five repeated experiments were conducted for each model. The EMs obtained from these experiments were statistically analyzed to compute their mean values and standard deviations. The summarized results are presented in Table 3. The results indicate that the stacking model produced the highest AUC (91.67%), slightly outperforming CNN (90.67%), while MLP exhibited the lowest value (88.83%). Additionally, the stacking model also recorded the highest values for OA at 83.69%, recall at 75.03%, F1 score at 82.35%, and kappa coefficient at 67.43%. These results confirm the stacking model's leading performance and support the predictive robustness of the subsequent partition-based models.

Table 3. Results of EMs for models. (The bolded and underlined value means the highest EMs of the column; percentages (%) are used to characterize each result.)

EMs **Models**	**AUC**	**OA**	**Precision**	**Recall**	**F1 Score**	**Kappa**	**MCC**
CNN	90.67 ± 0.80	83.56 ± 0.90	93.13 ± 3.64	73.54 ± 3.68	82.08 ± 1.68	67.27 ± 1.86	**69.01** ± 1.87
DNN	89.98 ± 1.15	82.46 ± 1.73	92.66 ± 5.55	72.09 ± 3.06	80.95 ± 2.14	65.18 ± 3.57	67.15 ± 4.10
MLP	88.83 ± 5.82	81.68 ± 1.99	**94.32** ± 4.73	68.55 ± 3.53	79.31 ± 2.79	63.54 ± 4.17	66.24 ± 4.74
Stacking	**91.67** ± 0.26	**83.69** ± 0.96	91.38 ± 1.62	**75.03** ± 3.12	**82.35** ± 1.58	**67.43** ± 1.91	68.62 ± 1.59

Subsequently, a systematic evaluation was conducted to assess how SHP and feature selection strategies influence the performance of four ensemble LSA models: stacking, F-stacking, H-stacking, and HF-stacking (see Figure 15). The HF-stacking model consistently outperformed the other models in all subregions, achieving the highest scores in OA, recall, F1 score, kappa, and MCC. Additionally, it demonstrated the largest coverage area in the radar chart analysis, further validating the model's superiority. Furthermore, incorporating feature selection contributed to a notable improvement in model performance. In the global analysis framework, the F-stacking model showed a remarkable performance improvement over the stacking model: OA reached 85.31% (an increase of 1.62%), precision reached 93.01% (an increase of 1.63%), recall improved to 76.60% (a 1.57% increase), and the F1 score rose to 84.00% (a 1.65% increase). The kappa coefficient (70.63%) and MCC (71.77%) also saw significant improvements of 3.20% and 3.15%, respectively. It is noteworthy that the SHP enabled the HF-stacking model to demonstrate comprehensive improvements compared to the H-stacking model, with all EMs showing significant enhancements.

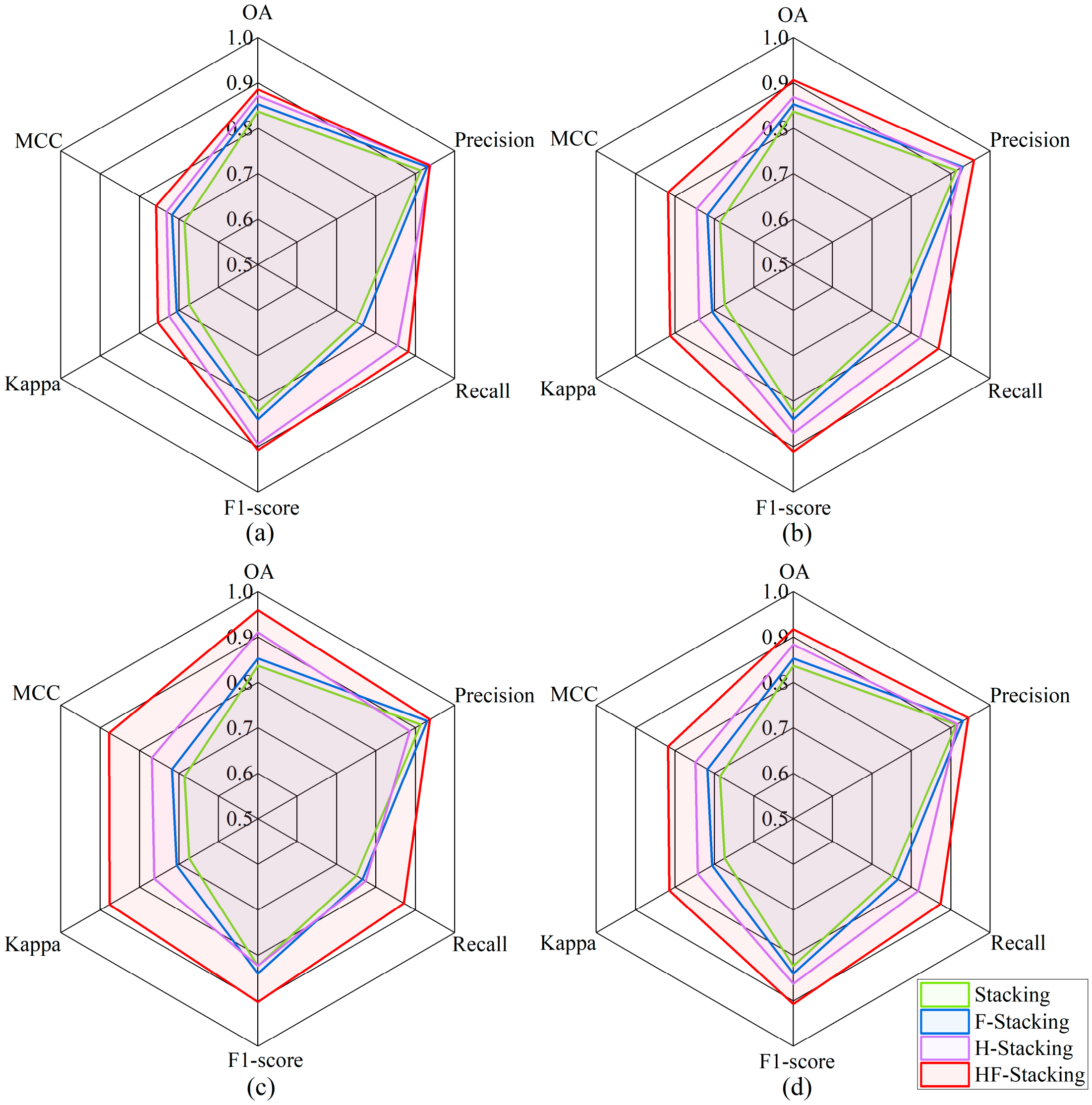

(a) (b) (c) (d)

Figure 15. Radar charts of EMs for the LSA models. (**a**) Radar chart for subregion I; (**b**) radar chart for subregion II; (**c**) radar chart for subregion III; (**d**) radar chart for average EMs across subregions.

Figure 15d illustrates the radar chart showing the mean EMs for subregions. Compared to the stacking model, the HF-stacking model achieved substantial gains in key metrics: OA increased by 8.01% to 91.70%, precision increased by 3.03% to 94.41%, F1 score grew by 8.36% to 90.71%, kappa rose by 14.01% to 81.44%, and MCC improved by 13.18% to 81.80%. These results convincingly demonstrate that constructing a framework for SHP and implementing regionally optimized feature selection strategies can effectively reduce the interference of spatial heterogeneity in global modeling. Consequently, this approach significantly enhances the predictive performance of LSA models.

5.2. Comparison of LSM for Typical Landslide Areas

To validate the reliability of the proposed model, this study selected the Laowang Mountain landslide—located in Pingzi Village, Qiaotou Township, Hekou County (centered at 104°6′50″E, 22°50′20″N)—as a representative case. This landslide is classified as a shallow landslide in terms of material thickness, a medium-sized earth slide in terms of volume, and a composite landslide due to the combined push and pull forces that triggered the movement. It demonstrates significant structural complexity and evolutionary representativeness. Notably, landslides in the study area are predominantly shallow, with soil-based sliding masses. The Laowang Mountain landslide closely reflects the regional landslide characteristics in terms of triggering mechanisms, morphological features, and material composition, making it a typical and representative case for model evaluation. It is located within a karstic mountainous zone shaped by long-term erosion, where the terrain generally inclines from south to north. The elevation spans from 1123.03 m at the landslide's rear to 1070.20 m at the front, yielding a vertical difference of about 52.83 m. The overall slope ranges from about 10° to 18°, with steep steps reaching heights of 1 to 5 m commonly observed on the slope surface. Figure 16a presents a Google satellite imagery interpretation of the Pingzi Village landslide, while Figure 16k showcases drone aerial photography from the field investigation. The landslide presents a tongue-shaped morphology, extending roughly 155–270 m in length and 123 m in width, with a surface area estimated at 27,700 m^2. The sliding direction is approximately 351°, with an average thickness of about 7.5 m, leading to a total volume of approximately 20.77×10^4 m^3.

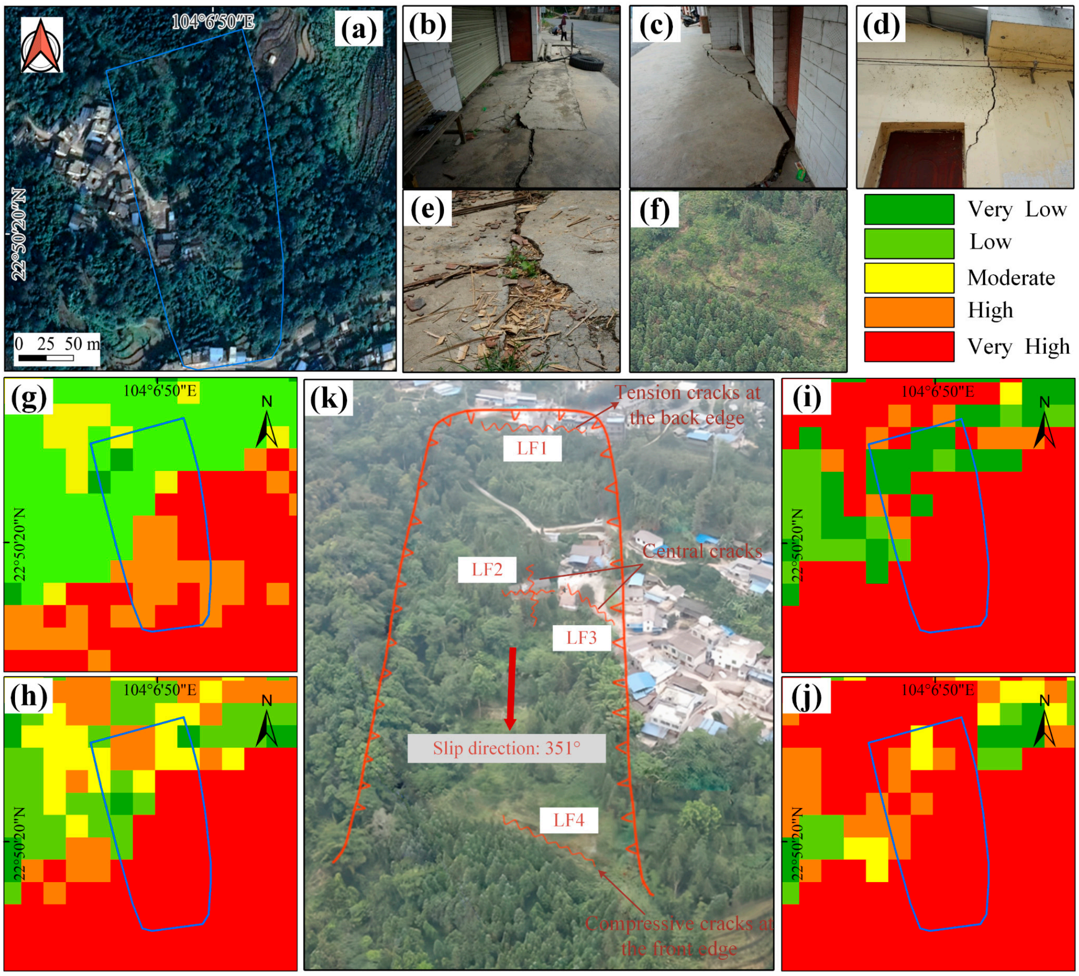

Figure 16. Analysis of model prediction results for typical landslide areas based on field investigation. (**a**) Interpretation map of landslide areas derived from Google satellite imagery; (**b**,**c**) field photographs of LF1; (**d**–**f**) field photographs of LF2, LF3, and LF4, respectively; (**g**–**j**) detailed views of the LSMs generated by the stacking, F-stacking, H-stacking, and HF-stacking models, respectively; (**k**) UAV photograph.

Field surveys and interviews revealed that the primary signs of deformation in this landslide include ground cracking, leading to the formation of fissures. Deformation began in August 2012 and has since developed four notable cracks, designated as LF1, LF2, LF3, and LF4. Relevant field photographs are shown in Figure 16b–f. LF1 is positioned at the southern residential area road, measuring about 50 m in length and 3 to 5 cm in width, with a distinct boundary. LF2, located near the activity room of the village in the central part of the landslide, is approximately 38 m long with surface cracks measuring 1 to 4 cm in width, causing damage to the walls of the activity room. LF3, which extends about 32 m in length, has surface cracks ranging from 3 to 8 cm wide, resulting in structural tilting and significant wall deformation in one residence, which has since required evacuation. LF4 measures around 12 m in length and features surface cracks 5 to 15 cm wide, with surface subsidence of 10 to 30 cm observed at this location. The landslide is currently in a creep phase, and given increased rainfall, additional artificial loading at the summit, and potential seismic activities, there is a significant risk of continued deformation and large-scale sliding.

A comparative analysis of the four integrated models—stacking, F-stacking, H-stacking, and HF-stacking—was conducted in relation to the LSM in this landslide area. The results indicate that the proposed HF-stacking model demonstrates a more comprehensive and consistent performance in accurately classifying the landslide area as "Very High". In contrast, while the other three models identified some "Very High" regions, they generally exhibited deficiencies, often including "Low" areas in their predictions. Thus, the HF-stacking model shows optimal performance in predicting the landslide areas. Furthermore, F-stacking and H-stacking models revealed higher accuracy in detailed predictions compared to the stacking model, suggesting that SHP and feature selection strategies provide significant advantages in enhancing the predictive capability of the model.

6. Conclusions

LSA provides an essential scientific foundation for landslide risk mitigation. This study proposes an innovative integrated approach that combines t-SNE for dimensionality reduction with ISO clustering, utilizing LCFs and landslide inventory data. This method effectively mitigates the impact of spatial heterogeneity on assessment results. Furthermore, by incorporating a feature selection strategy, the model exhibited notable enhancements in both forecast precision and stability. The main conclusions of this research are outlined below:

(1) Using the LCFs and inventory data from the study area, three DL models—CNN, DNN, and MLP—were developed. Utilizing the stacking ensemble method to integrate these models, we compared seven EMs, including AUC, OA, precision, and recall. The findings indicate that the stacking ensemble approach outperforms each individual model in terms of prediction accuracy;

(2) The t-SNE-ISO algorithm was employed to implement SHP within the study area. Simultaneously, feature selection strategies were applied to optimize the feature combinations, resulting in the construction of the HF-stacking model. This model effectively mitigates the biases in predictions caused by spatial heterogeneity and feature redundancy. The HF-stacking model consistently outperformed other models across multiple subregions, with notable enhancements in key performance metrics compared to the standard stacking approach;

(3) The F-stacking model significantly outperforms the traditional stacking model, with improvements of 1.62% in OA, 1.63% in precision, 1.57% in recall, and 1.65% in F1 score. Additionally, the kappa coefficient and MCC increased by 3.20% and 3.15%, respectively. Furthermore, the HF-stacking model exhibited comprehensive improvements compared to the H-stacking model, with all EMs significantly enhanced;

(4) These findings provide strong evidence that establishing an SHP framework and implementing feature selection strategies can effectively reduce the effects of spatial heterogeneity and feature redundancy, thereby significantly improving the accuracy and predictive performance of LSA.

Author Contributions: Conceptualization, X.J., Z.Y. and H.M.; methodology, Z.Y., X.J. and M.Z.; software, X.J. and M.Z.; formal analysis, Z.Y., H.M. and J.Y.; data curation, X.J., Z.Y. and H.M.; writing—original draft preparation, X.J. and Z.Y.; writing—review and editing, H.M., M.Z., J.Y. and L.W.; project administration, Z.Y.; funding acquisition, Z.Y., X.J. and L.W. All authors have read and agreed to the published version of the manuscript.

Funding: This research was funded by the Natural Science Research Project of Anhui Educational Committee (Grant NO. 2024AH050384), the Graduate Innovation Fund Project of Anhui University of Science and Technology (Grant NO. 2024cx2148), the Coal Industry Engineering Research Center of Mining Area Environmental and Disaster Cooperative Monitoring (Anhui University of Science and Technology) (Grant NO. KSXTJC202304), the Key Laboratory of Aviation-aerospace-ground Cooperative Monitoring and Early Warning of Coal Mining-induced Disasters of Anhui Higher Education Institutes (Anhui University of Science and Technology) (Grant NO. KLAHEI202208), and the National Natural Science Foundation of China (Grant NO. 52474194).

Data Availability Statement: The data supporting the findings of this study are available from the corresponding author upon reasonable request.

Acknowledgments: The authors would like to thank the ESA for providing the Sentinel-1 SAR data and the Alaska Satellite Facility (ASF) for data distribution (https://search.asf.alaska.edu/ (accessed on 20 December 2024)). The authors are also grateful to the LiDAR Research Group of Peking University for providing the S1IP software (https://sarimggeodesy.github.io/ (accessed on 12 June 2023)).

Conflicts of Interest: The authors declare no conflicts of interest.

References

1. Gu, T.; Duan, P.; Wang, W.; Li, J.; Li, S. Review of methods for landslide susceptibility assessment. *J. Nat. Disasters* **2024**, *33*, 1–16.
2. Wang, J.; Wang, Y.; Li, M.; Qi, Z.; Li, C.; Qi, H.; Zhang, X. Improved landslide susceptibility assessment: A new negative sample collection strategy and a comparative analysis of zoning methods. *Ecol. Indic.* **2024**, *169*, 112948. [CrossRef]
3. Yu, H.; Pei, W.; Zhang, J.; Chen, G. Landslide Susceptibility Mapping and Driving Mechanisms in a Vulnerable Region Based on Multiple Machine Learning Models. *Remote Sens.* **2023**, *15*, 1886. [CrossRef]
4. Mersha, T.; Meten, M. GIS-based landslide susceptibility mapping and assessment using bivariate statistical methods in Simada area, northwestern Ethiopia. *Geoenviron. Disasters* **2020**, *7*, 20. [CrossRef]
5. Wu, Y.; Li, W.; Wang, Q.; Liu, Q.; Yang, D.; Xing, M.; Pei, Y.; Yan, S. Landslide susceptibility assessment using frequency ratio, statistical index and certainty factor models for the Gangu County, China. *Arab. J. Geosci.* **2016**, *9*, 84. [CrossRef]
6. Tang, Y.; Feng, F.; Guo, Z.; Feng, W.; Li, Z.; Wang, J.; Sun, Q.; Ma, H.; Li, Y. Integrating principal component analysis with statistically-based models for analysis of causal factors and landslide susceptibility mapping: A comparative study from the loess plateau area in Shanxi (China). *J. Clean. Prod.* **2020**, *277*, 124159. [CrossRef]
7. Qin, Y.; Zhao, Z.; Zhou, D.; Chang, K.; Mou, Q.; Yang, Y.; Hu, Y. Landslide Susceptibility Assessment in Yulong County Using Contribution Degree Clustering Method and Stacking Ensemble Coupled Model Based on Certainty Factor. *Remote Sens.* **2024**, *16*, 3582. [CrossRef]
8. Wubalem, A. Landslide susceptibility mapping using statistical methods in Uatzau catchment area, northwestern Ethiopia. *Geoenviron. Disasters* **2021**, *8*, 1. [CrossRef]
9. Vaka, D.S.; Yaragunda, V.R.; Perdikou, S.; Papanicolaou, A. InSAR Integrated Machine Learning Approach for Landslide Susceptibility Mapping in California. *Remote Sens.* **2024**, *16*, 3574. [CrossRef]
10. Agboola, G.; Beni, L.H.; Elbayoumi, T.; Thompson, G. Optimizing landslide susceptibility mapping using machine learning and geospatial techniques. *Ecol. Inf.* **2024**, *81*, 102583. [CrossRef]
11. Wang, Y.; Fang, Z.; Hong, H. Comparison of convolutional neural networks for landslide susceptibility mapping in Yanshan County, China. *Sci. Total Environ.* **2019**, *666*, 975–993. [CrossRef] [PubMed]
12. Hussain, M.A.; Chen, Z.; Zheng, Y.; Zhou, Y.; Daud, H. Deep Learning and Machine Learning Models for Landslide Susceptibility Mapping with Remote Sensing Data. *Remote Sens.* **2023**, *15*, 4703. [CrossRef]
13. Meghanadh, D.; Kumar Maurya, V.; Tiwari, A.; Dwivedi, R. A multi-criteria landslide susceptibility mapping using deep multi-layer perceptron network: A case study of Srinagar-Rudraprayag region (India). *Adv. Space Res.* **2022**, *69*, 1883–1893. [CrossRef]

14. Gao, B.; He, Y.; Chen, X.; Chen, H.; Yang, W.; Zhang, L. A Deep Neural Network Framework for Landslide Susceptibility Mapping by Considering Time-Series Rainfall. *IEEE J. Sel. Top. Appl. Earth Obs. Remote Sens.* **2024**, *17*, 5946–5969. [CrossRef]
15. Wang, J.; Wang, Y.; Li, C.; Li, Y.; Qi, H. Landslide susceptibility evaluation based on landslide classification and ANN-NFR modelling in the Three Gorges Reservoir area, China. *Ecol. Indic.* **2024**, *160*, 111920. [CrossRef]
16. Zhang, Q.; He, Y.; Zhang, Y.; Lu, J.; Zhang, L.; Huo, T.; Tang, J.; Fang, Y.; Zhang, Y. A Graph–Transformer Method for Landslide Susceptibility Mapping. *IEEE J. Sel. Top. Appl. Earth Obs. Remote Sens.* **2024**, *17*, 14556–14574. [CrossRef]
17. Aslam, B.; Zafar, A.; Khalil, U. Comparative analysis of multiple conventional neural networks for landslide susceptibility mapping. *Nat. Hazard.* **2023**, *115*, 673–707. [CrossRef]
18. Zhang, S.; Bai, L.; Li, Y.; Li, W.; Xie, M. Comparing Convolutional Neural Network and Machine Learning Models in Landslide Susceptibility Mapping: A Case Study in Wenchuan County. *Front. Environ. Sci.* **2022**, *10*, 886841. [CrossRef]
19. Gao, B.; He, Y.; Chen, X.; Zheng, X.; Zhang, L.; Zhang, Q.; Lu, J. Landslide Risk Evaluation in Shenzhen Based on Stacking Ensemble Learning and InSAR. *IEEE J. Sel. Top. Appl. Earth Obs. Remote Sens.* **2023**, *16*, 1–18. [CrossRef]
20. He, Y.; Huo, T.; Gao, B.; Zhu, Q.; Jin, L.; Chen, J.; Zhang, Q.; Tang, J. Thaw Slump Susceptibility Mapping Based on Sample Optimization and Ensemble Learning Techniques in Qinghai-Tibet Railway Corridor. *IEEE J. Sel. Top. Appl. Earth Obs. Remote Sens.* **2024**, *17*, 5443–5459. [CrossRef]
21. Hong, H. Assessing landslide susceptibility based on hybrid Best-first decision tree with ensemble learning model. *Ecol. Indic.* **2023**, *147*, 109968. [CrossRef]
22. Wu, X.; Wang, J. Application of Bagging, Boosting and Stacking Ensemble and EasyEnsemble Methods for Landslide Susceptibility Mapping in the Three Gorges Reservoir Area of China. *Int. J. Environ. Res. Public Health* **2023**, *20*, 4977. [CrossRef]
23. Zhou, C.; Gan, L.; Wang, Y.; Wu, H.; Yu, J.; Cao, Y.; Yin, K. Landslide Susceptibility Prediction based on Non-Landslide Samples Selection and Heterogeneous Ensemble Machine Learning. *J. Geo-Inf. Sci.* **2023**, *25*, 1570–1585.
24. Wu, L.; Zeng, T.; Liu, X.; Guo, Z.; Liu, Z.; Yin, K. Landslide Susceptibility Assessment Based on Ensemble Learning Modeling. *Earth Sci.* **2024**, *49*, 3841–3854.
25. Wang, Y.; Cao, Y.; Xu, F.; Zhou, C.; Yu, L.; Wu, L.; Wang, Y.; Yin, K. Reservoir Landslide Susceptibility Prediction Considering Non-Landslide Sampling and Ensemble Machine Learning Methods. *Earth Sci.* **2024**, *49*, 1619–1635.
26. Zhu, S.; Kong, R.; Luo, X.; Xu, Z.; Zhu, F. An improved potential landslide hazard points evaluating method considering the heterogeneity of environmental features. *Int. J. Environ. Sci. Technol.* **2023**, *20*, 7951–7968. [CrossRef]
27. Chang, Z.; Catani, F.; Huang, F.; Liu, G.; Meena, S.R.; Huang, J.; Zhou, C. Landslide susceptibility prediction using slope unit-based machine learning models considering the heterogeneity of conditioning factors. *J. Rock Mech. Geotech. Eng.* **2023**, *15*, 1127–1143. [CrossRef]
28. Liu, Y.; Chen, C. Landslide susceptibility evaluation method considering spatial heterogeneity and feature selection. *Acta Geod. Et Cartogr. Sin.* **2024**, *53*, 1417–1428.
29. Aggarwal, C.C.; Yu, P.S.; Han, J.; Wang, J. A Framework for Clustering Evolving Data Streams. In Proceedings of the Proceedings 2003 VLDB Conference, Berlin, Germany, 9–12 September 2003; pp. 81–92.
30. Althuwaynee, O.F.; Aydda, A.; Hwang, I.-T.; Lee, Y.-K.; Kim, S.-W.; Park, H.-J.; Lee, M.-S.; Park, Y. Uncertainty Reduction of Unlabeled Features in Landslide Inventory Using Machine Learning t-SNE Clustering and Data Mining Apriori Association Rule Algorithms. *Appl. Sci.* **2021**, *11*, 556. [CrossRef]
31. Chen, X.; Chen, W. GIS-based landslide susceptibility assessment using optimized hybrid machine learning methods. *CATENA* **2021**, *196*, 104833. [CrossRef]
32. Shen, Z.; Wang, D.; Arabameri, A.; Santosh, M.; Egbueri, J.C.; Arora, A. Landslide susceptibility assessment and mapping using new ensemble model. *Adv. Space Res.* **2024**, *74*, 2859–2882. [CrossRef]
33. Lu, J.; Yi, H.; Lifeng, Z.; Qing, Z.; Binghai, G.; Hesheng, C.; Fang, Y. Ensemble learning landslide susceptibility assessment with optimized non-landslide samples selection. *Geomat. Nat. Hazards Risk* **2024**, *15*, 2378176. [CrossRef]
34. Wen, H.; Liu, B.; Di, M.; Li, J.; Zhou, X. A SHAP-enhanced XGBoost model for interpretable prediction of coseismic landslides. *Adv. Space Res.* **2024**, *74*, 3826–3854. [CrossRef]
35. Gu, T.; Li, J.; Wang, M.; Duan, P.; Zhang, Y.; Cheng, L. Study on landslide susceptibility mapping with different factor screening methods and random forest models. *PLoS ONE* **2023**, *18*, e0292897. [CrossRef] [PubMed]
36. Wang, Y.; Wu, X.; Chen, Z.; Ren, F.; Feng, L.; Du, Q. Optimizing the Predictive Ability of Machine Learning Methods for Landslide Susceptibility Mapping Using SMOTE for Lishui City in Zhejiang Province, China. *Int. J. Environ. Res. Public Health* **2019**, *16*, 368. [CrossRef]
37. Lv, J.; Zhang, R.; Shama, A.; Hong, R.; He, X.; Wu, R.; Bao, X.; Liu, G. Exploring the spatial patterns of landslide susceptibility assessment using interpretable Shapley method: Mechanisms of landslide formation in the Sichuan-Tibet region. *J. Environ. Manag.* **2024**, *366*, 121921. [CrossRef]
38. Zhang, L.; Guo, Z.; Qi, S.; Zhao, T.; Wu, B.; Li, P. Landslide susceptibility evaluation and determination of critical influencing factors in eastern Sichuan mountainous area, China. *Ecol. Indic.* **2024**, *169*, 112911. [CrossRef]

39. Youssef, K.; Shao, K.; Moon, S.; Bouchard, L.S. Landslide susceptibility modeling by interpretable neural network. *Commun. Earth Environ.* **2023**, *4*, 162. [CrossRef]
40. Cao, C.; Zhu, K.; Xu, P.; Shan, B.; Yang, G.; Song, S. Refined landslide susceptibility analysis based on InSAR technology and UAV multi-source data. *J. Clean. Prod.* **2022**, *368*, 133146. [CrossRef]
41. Li, J.; Zhou, C. Appropriate Grid Size for Terrain Based Landslide Risk Assessment in Lantau Island, Hong Kong. *J. Remote Sens.* **2003**, *7*, 86–92+161. [CrossRef]
42. Wang, Y.; Feng, L.; Li, S.; Ren, F.; Du, Q. A hybrid model considering spatial heterogeneity for landslide susceptibility mapping in Zhejiang Province, China. *CATENA* **2020**, *188*, 104425. [CrossRef]
43. Hooper, A.; Zebker, H.; Segall, P.; Kampes, B. A new method for measuring deformation on volcanoes and other natural terrains using InSAR persistent scatterers. *Geophys. Res. Lett.* **2004**, *31*, L23611. [CrossRef]
44. Van der Maaten, L.; Hinton, G. Viualizing data using t-SNE. *J. Mach. Learn. Res.* **2008**, *9*, 2579–2605.
45. Rane, P.R.; Vincent, S. Landslide Susceptibility Mapping Using Machine Learning Algorithms for Nainital, India. *Eng. Sci.* **2022**, *17*, 142–155. [CrossRef]
46. Zhou, X.; Wen, H.; Zhang, Y.; Xu, J.; Zhang, W. Landslide susceptibility mapping using hybrid random forest with GeoDetector and RFE for factor optimization. *Geosci. Front.* **2021**, *12*, 101211. [CrossRef]
47. Wang, Y.; Wen, H.; Sun, D.; Li, Y. Quantitative Assessment of Landslide Risk Based on Susceptibility Mapping Using Random Forest and GeoDetector. *Remote Sens.* **2021**, *13*, 2625. [CrossRef]
48. Cun, Y.L.; Boser, B.; Denker, J.S.; Henderson, D.; Jackel, L.D. Handwritten digit recognition with a back-propagation network. *Adv. Neural Inf. Process. Syst.* **1990**, *2*, 396–404.
49. Chen, Y.; Ming, D.; Yu, J.; Xu, L.; Ma, Y.; Li, Y.; Ling, X.; Zhu, Y. Susceptibility-Guided Landslide Detection Using Fully Convolutional Neural Network. *IEEE J. Sel. Top. Appl. Earth Obs. Remote Sens.* **2023**, *16*, 998–1018. [CrossRef]
50. Zhao, Z.; Chen, T.; Dou, J.; Liu, G.; Plaza, A. Landslide Susceptibility Mapping Considering Landslide Local-Global Features Based on CNN and Transformer. *IEEE J. Sel. Top. Appl. Earth Obs. Remote Sens.* **2024**, *17*, 7475–7489. [CrossRef]
51. Jiang, Z.; Wang, M.; Liu, K. Comparisons of Convolutional Neural Network and Other Machine Learning Methods in Landslide Susceptibility Assessment: A Case Study in Pingwu. *Remote Sens.* **2023**, *15*, 798. [CrossRef]
52. Zhao, Z.; He, Y.; Yao, S.; Yang, W.; Wang, W.; Zhang, L.; Sun, Q. A comparative study of different neural network models for landslide susceptibility mapping. *Adv. Space Res.* **2022**, *70*, 383–401. [CrossRef]
53. Yang, Z.; Xu, C.; Shao, X.; Ma, S.; Li, L. Landslide susceptibility mapping based on CNN-3D algorithm with attention module embedded. *Bull. Eng. Geol. Environ.* **2022**, *81*, 412. [CrossRef]
54. Hinton, G.E.; Osindero, S.; Teh, Y.-W. A Fast Learning Algorithm for Deep Belief Nets. *Neural Comput.* **2006**, *18*, 1527–1554. [CrossRef] [PubMed]
55. Mwakapesa, D.S.; Lan, X.; Mao, Y. Landslide susceptibility assessment using deep learning considering unbalanced samples distribution. *Heliyon* **2024**, *10*, e30107. [CrossRef] [PubMed]
56. Ma, W.; Dong, J.; Wei, Z.; Peng, L.; Wu, Q.; Wang, X.; Dong, Y.; Wu, Y. Landslide susceptibility assessment using the certainty factor and deep neural network. *Front. Earth Sci.* **2023**, *10*, 1091560. [CrossRef]
57. Dou, J.; Yunus, A.P.; Merghadi, A.; Shirzadi, A.; Nguyen, H.; Hussain, Y.; Avtar, R.; Chen, Y.; Pham, B.T.; Yamagishi, H. Different sampling strategies for predicting landslide susceptibilities are deemed less consequential with deep learning. *Sci. Total Environ.* **2020**, *720*, 137320. [CrossRef] [PubMed]
58. Wang, Y.; Zhou, C.; Cao, Y.; Meena, S.R.; Feng, Y.; Wang, Y. Utilizing deep learning approach to develop landslide susceptibility mapping considering landslide types. *Bull. Eng. Geol. Environ.* **2024**, *83*, 430. [CrossRef]
59. Liu, X.K.; Shao, S.; Shao, S.J. Landslide susceptibility prediction and mapping in Loess Plateau based on different machine learning algorithms by hybrid factors screening: Case study of Xunyi County, Shaanxi Province, China. *Adv. Space Res.* **2024**, *74*, 192–210. [CrossRef]
60. Song, Y.; Song, Y.X.; Wang, C.N.; Wu, L.W.; Wu, W.C.; Li, Y.; Li, S.C.; Chen, A.Q. Landslide susceptibility assessment through multi-model stacking and meta-learning in Poyang County, China. *Geomat. Nat. Hazards Risk* **2024**, *15*, 2354499. [CrossRef]
61. Yu, L.; Wang, Y.; Pradhan, B. Enhancing landslide susceptibility mapping incorporating landslide typology via stacking ensemble machine learning in Three Gorges Reservoir, China. *Geosci. Front.* **2024**, *15*, 101802. [CrossRef]
62. Mebirouk, N.; Amrane, M.; Messast, S. Optimizing Landslide Susceptibility Mapping in Oued Guebli Watershed: A Comparative Study of Deep Learning, Support Vector Machines, Logistic Regression with Spatial Validation and AUC-ROC Analysis. *Iran. J. Sci. Technol.-Trans. Civ. Eng.* **2025**. [CrossRef]